PNAS RESEARCH ARTICLE | DEVELOPMENTAL BIOLOGY

Ancient vertebrate dermal armor evolved from trunk neural crest

Jan Stundl[a,b,1], Megan L. Martik[a,2,3], Donglei Chen[c,2], Desingu Ayyappa Raja[a,2], Roman Franěk[b], Anna Pospisilova[d], Martin Pšenička[b], Brian D. Metscher[e], Ingo Braasch[f,g], Tatjana Haitina[c], Robert Cerny[d], Per E. Ahlberg[c], and Marianne E. Bronner[a,1]

Edited by Neil Shubin, The University of Chicago, Chicago, IL; received December 15, 2022; accepted April 26, 2023

Bone is an evolutionary novelty of vertebrates, likely to have first emerged as part of ancestral dermal armor that consisted of osteogenic and odontogenic components. Whether these early vertebrate structures arose from mesoderm or neural crest cells has been a matter of considerable debate. To examine the developmental origin of the bony part of the dermal armor, we have performed in vivo lineage tracing in the sterlet sturgeon, a representative of nonteleost ray-finned fish that has retained an extensive postcranial dermal skeleton. The results definitively show that sterlet trunk neural crest cells give rise to osteoblasts of the scutes. Transcriptional profiling further reveals neural crest gene signature in sterlet scutes as well as bichir scales. Finally, histological and microCT analyses of ray-finned fish dermal armor show that their scales and scutes are formed by bone, dentin, and hypermineralized covering tissues, in various combinations, that resemble those of the first armored vertebrates. Taken together, our results support a primitive skeletogenic role for the neural crest along the entire body axis, that was later progressively restricted to the cranial region during vertebrate evolution. Thus, the neural crest was a crucial evolutionary innovation driving the origin and diversification of dermal armor along the entire body axis.

neural crest | vertebrate evolution | scales | sterlet sturgeon | skeleton

The evolutionary success of vertebrates is intimately associated with acquisition of the neural crest (NC), a stem-cell population with remarkable migratory potential and the ability to form a vast array of derivatives (1, 2). NC cells arise in the developing embryo within the forming central nervous system, then migrate away throughout the periphery and form diverse cell types, ranging from ectomesenchymal elements of the craniofacial skeleton to most of the peripheral nervous system (3). However, there are differences in NC cells along the body axis. For example, in birds and mammals, only the cranial NC has the ability to form ectomesenchymal cartilage and bone in vivo. While trunk NC cells normally lack this ability, they can be reprogrammed to do so using cranial crest transcription factors (4) or other experimental manipulations (5, 6). Moreover, single-cell analysis of murine NC has revealed promesenchymal bias in trunk NC cells such that overexpression of *Twist1* can shift them toward ectomesenchymal fates (7).

The entire body of most nontetrapod vertebrates is covered with various dermal mineralized structures (8). This extensive dermal armor consists of either bone (osteogenic unit), dentin (odontogenic unit), or both tissues. During the course of vertebrate evolution, differential combinations of loss and/or retention of dentinous and bony components led to an enormous diversity of scales, scutes, and denticles in vertebrate lineages (9, 10). The head-to-tail distribution of the dermal armor has prompted discussion regarding the intriguing possibility that skeletogenic potential may have been present in NC cells along the entire body axis of gnathostome ancestors (10). During the transition of tetrapods to land, the odontogenic and osteogenic dermal armor units were gradually reduced, including the loss of dental ornament and the replacement of the thick bony base by a weakly mineralized plywood-like structure in the sarcopterygian elasmoid scales (11) as in teleosts. Thus, the skeletogenic ability of the NC likely became gradually restricted to the head, by spatiotemporal changes in some gene regulatory network (GRN) components (12). To date, the developmental evidence regarding the skeletogenic ability of the trunk NC remains sparse. Lineage tracing in the little skate has suggested that trunk NC cells have the ability to give rise to dermal denticles (13), which are dentinous structures that cover the entire body. This and other evidence strongly suggest that the odontoblast program was ancestrally associated with the NC along the entire anterior-to-posterior (AP) body axis (14). However, whether trunk NC has the potential to form osteogenic components lacks hard evidence.

While the modern chondrichthyan exoskeleton only retains odontogenic components, the dermal armor of primitive vertebrates typically was either comprised of dentin units that

Significance

The body of early vertebrates was covered from the head to tail with extensive dermal armor, comprised of dentin and bone. There has long been controversy over whether this armor arose from the neural crest, mesoderm, or both. Since odontoblasts (dentin-producing cells) are exclusively neural crest derived, we probed the developmental origin of the bony component of the dermal armor in the sterlet sturgeon, an early branching lineage of ray-finned fishes. Here, we show that trunk neural crest of the sterlet gives rise to osteoblasts, producing the bone of the scutes. Together, our results support a primitive skeletogenic role for the neural crest along the entire body axis, that was later progressively restricted to the cranial region during vertebrate evolution.

Author contributions: J.S., P.E.A., and M.E.B. designed research; J.S., M.L.M., D.C., D.A.R., and R.F. performed research; J.S., D.C., A.P., M.P., I.B., T.H., and R.C. contributed new reagents/analytic tools; J.S., M.L.M., D.C., D.A.R., R.F., and B.D.M. analyzed data; and J.S., D.C., P.E.A., and M.E.B. wrote the paper.

The authors declare no competing interest.

This article is a PNAS Direct Submission.

[1]To whom correspondence may be addressed. Email: jstundl@caltech.edu or mbronner@caltech.edu.

[2]M.L.M., D.C., and D.A.R. contributed equally to this work.

[3]Present address: Department of Molecular and Cell Biology, University of California, Berkeley, CA 94720.

This article contains supporting information online at https://www.pnas.org/lookup/suppl/doi:10.1073/pnas.2221120120/-/DCSupplemental.

Published July 17, 2023.

rested on dermal bones, or solely consisted of osteogenic components as in some extinct jawless fishes (15, 16). In zebrafish and medaka scales (17–19), the plywood-like osteogenic layer has been shown to be derived from mesoderm, refuting earlier studies claiming an NC origin (20, 21). This has led to the suggestion that the odontogenic layer of the dermal exoskeleton comes from trunk NC, while the osteogenic layer arises from paraxial mesoderm (13). A complication is that teleost elasmoid scales are highly derived relative to the ancestral condition, such that zebrafish or medaka may not be appropriate model organisms for evaluating the broader evolutionary pattern of ectomesenchymal potential of the trunk NC.

To definitively examine whether the osteogenic component of the ancient dermal armor was trunk NC- or mesoderm-derived, here, we perform histological analysis on the dermal armor of the major phylogenetic lineages of ray-finned fishes (cladistians: bichir; chondrosteans: sterlet; holosteans: gar; and teleosts: armored catfish). Among them, sturgeons are a deep branch of ray-finned fishes, appearing in the fossil record from the Cretaceous (22, 23). They have a characteristic morphology with a long rostrum, reduced ossification of the endoskeleton, and an extensive dermal exoskeleton consisting of several types of scutes (24, 25). While sturgeon scutes likely evolved from ganoid scales (8), they have lost both ganoin (a multilayered ename) (26) and dentin. This makes them particularly useful for investigating potential NC involvement in the formation of trunk dermal bones. Therefore, we perform lineage tracing and RNA-seq analyses of the sterlet sturgeon (*Acipenser ruthenus* Linnaeus, 1758) to reveal whether trunk NC plays a role in the development of the bony part of the dermal armor.

Results and Discussion

Dermal Armor of Extant Ray-Finned Fishes. The ray-finned fishes are remarkably diversified, representing about half of all extant vertebrates. Because several lineages retain dermal armor with clearly identifiable dentinous and osteogenic components (8, 15), ray-finned fishes are poised to provide important insights into the evolutionary origin of dermal armor and the NC's ectomesenchymal potential. Particularly relevant species are nonteleosteans, such as bichirs, sturgeons, and gars, which represent early diverging groups of ray-finned fishes that may reflect ancestral conditions of bony fishes (including tetrapods). To this end, we compared the dermal exoskeleton in representatives of all major ray-finned fish lineages by examining the bony scutes of sterlet sturgeon (Chondrostei), the ganoid scales of Senegal bichir (Cladistia) and the spotted gar (Holostei), and the dermal armor of the bristlenose catfish (Teleostei) (Fig. 1*A*). We first used Alizarin Red for histological detection of mineralized structures (Fig. 1 *B*–*I*^{i} and *SI Appendix*, Fig. S1). For closer examination of individual scales and scutes, we used 3D histology based on microCT (Fig. 1 *J*–*M*) and resin-based histology (Fig. 1 *N*–*U*).

For bichir scales, our data show that they resemble the ancestral rhomboid scales of early osteichthyans with a bony plate, dentin, and a superficial layer of ganoin (Fig. 1 *J* and *N*–*O*), consistent with previous studies (27–29). The entire scale is interlaced with a dense vascularization system (Fig. 1*J*, *SI Appendix*, Fig. S2, and Movie S1). Our findings show that bichir scales are formed at least in part by trunk NC cells, which are clearly involved in dentin formation; whether NC is also involved in bony base formation is less clear (Fig. 1 *N*–*O* and *SI Appendix*, Fig. S2).

Gar scales are composed of a thick bony plate covered by a ganoin layer without dentin in between (Fig. 1 *L*–*R*). Nevertheless, dentin is involved in the morphogenesis of the gar exoskeleton, in the form of small acrodin-capped denticles (27, 30), arising on the scale surface prior to full mineralization of ganoin (Fig. 1 *H*^{i}, *L*, and *R*, *SI Appendix*, Fig. S3, and Movie S4). Interestingly, we found similar denticles on bichir ganoid scales near the anal fin (*SI Appendix*, Fig. S1*D*), and Hertwig (27) described them in the region of bichir pectoral fins. Although gar ganoid scales lack the dentin layer, the presence of denticles agrees with the hypothesis that trunk NC cells participate in the formation of gar dermal armor.

Denticles are also a key component of the armored catfish dermal exoskeleton (Fig. 1 *E*–*U*). They form sequentially at the posterior edge of the scutes (*SI Appendix*, Fig. S4, Oa-Od), composed of a cone of dentin covered by a cap of acrodin, and anchored to the underlying bone by a pedicle and ligament (Fig. 1 *M*–*U*, *SI Appendix*, Fig. S4, and Movie S2). Given the tooth-like composition and similar development to odontogenesis (31), this is also consistent with the idea that trunk NC cells participate in the development of armored catfish dermal exoskeleton. It is worth noting that while catfishes lost their scales during evolution (32), armored catfishes secondarily developed an extensive dermal exoskeleton (33), perhaps due to the reactivation of an ancestral developmental program within the trunk NC.

Collectively, these findings suggest that trunk NC has at least odontogenic potential across the ray-finned fishes and participates in the formation of remarkably diverse dermal armor. However, the embryonic origin of osteogenic unit of dermal armor remains unexplored.

The sterlet dermal exoskeleton is comprised of several types of scutes varying in size and shape (24, 25). First to arise are the dorsal scutes which extend from the head to far into the trunk region. Subsequently, four rows of lateral and ventral scutes appear with scattered tiny scutes between them (Fig. 1 *C*–*G*^{i}). The dorsal scutes are comprised of only cellular bone, forming a longitudinal crest which is higher in its hind part (Fig. 1 *K*–*P*^{ii} and *SI Appendix*, Fig. S5), with vascularization confined to one central canal (Fig. 1*K*, *SI Appendix*, Fig. S5, and Movie S3). These scutes lack dentin or hypermineralized layers, which makes them particularly useful for investigating potential NC involvement in the formation of trunk dermal bones.

Trunk NC Gives Rise to Osteoblasts in Sturgeon. As a first step in examining a possible NC contribution to scutes, we analyzed the spatiotemporal expression of the NC specifier gene *foxd3* in the sterlet embryo to determine the time course of its appearance. The first emigrating trunk NC cells were observed at stage 25 undergoing an epithelial-to-mesenchymal transition in the dorsal part of the neural tube (Fig. 2 *A*–*A*^{ii}). Thus, we chose stage 24 for focal microinjection of the fluorescent dye CM-DiI into the lumen and dorsal midline of the neural tube to label emigrating trunk NC cells and test their ability to contribute to the dorsal bony scutes of sterlet (Fig. 2*B* and *SI Appendix*, Fig. S6 *A*–*A*^{i}). One day postinjection, we observed labeled trunk NC cells migrating around the somites similar to other vertebrates (Fig. 2 *C*–*C*^{i} and *SI Appendix*, Fig. S6 *B*–*B*^{i}). To examine the long-term fate of these trunk NC cells, embryos were allowed to develop to 22 to 23 mm (Fig. 2 *D* and *D*^{i}), by which mineralization of the dorsal scutes had initiated. Histological examination revealed CM-DiI-positive cells located in the dorsal root ganglia (Fig. 2*D*^{ii}), an expected trunk NC derivative. Importantly, dye-labeled cells were observed around the bone forming in the scute (n = 44) (Fig. 2*D*^{iii} and *SI Appendix*, Fig. S6). While the majority of CM-DiI-labeled cells were located in the ventral part of the scute, there was also label in the dorsal part tightly associated with the bone (Fig. 2 *D*^{iii}–*F*^{i} and *SI Appendix*, Fig. S6 *F*–*I*^{i}).

To address the possibility that some CM-DiI-positive cells are osteoblasts, we performed hybridization chain reaction (HCR), a highly sensitive in situ hybridization technique, to examine the

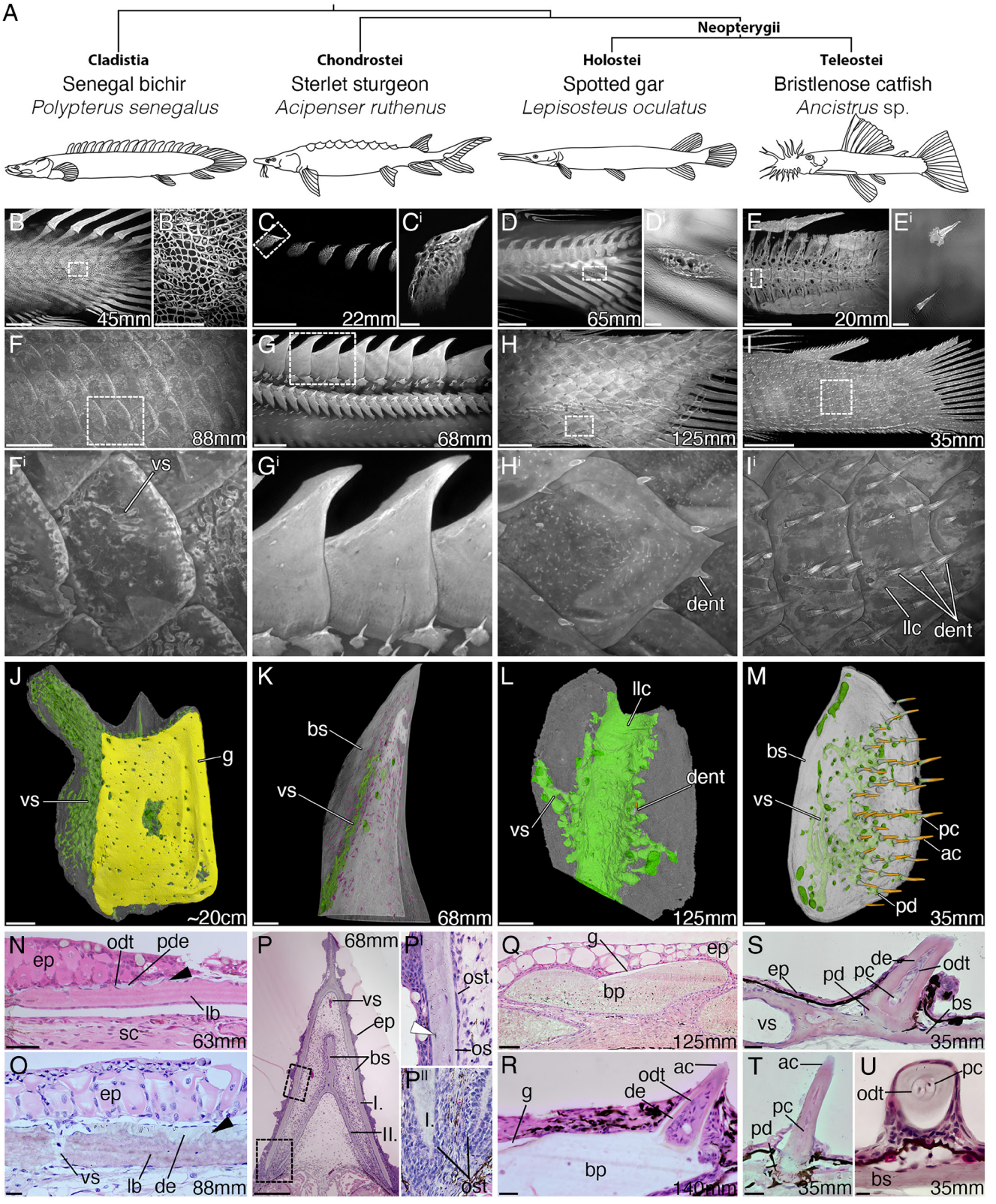

Fig. 1. Ray-finned fishes exhibit a remarkably diversified dermal exoskeleton. (*A*) Simplified phylogeny of ray-finned fishes highlighting studied species. (*B–I*^{i}) Alizarin Red showing the first developed scales and scutes (*B–E*^{i}), and the general morphology of the dermal exoskeleton in bichir (*B–F*^{i}), sterlet (*C–G*^{i}), gar (*D–H*^{i}), and armored catfish (*E–I*^{i}). (*J–M*) microCT reconstructions of single scale of bichir (*J*), gar (*L*), scute of sterlet (*K*), and catfish (*M*). The green corresponds to vascularization (vs), magenta to osteocytes, yellow to ganoin (g), and gold to acrodin (ac). bs, bony scute; dent, denticle; llc, lateral line canal; pc, pulp cavity. (*N–U*) Transverse sections reveal details of internal morphology of individual scales and scutes. Black arrowheads mark the ornamented outer layer of the scale. White arrowheads mark osteocytes. bp, bony plate; de, dentin; ep, epidermis; lb, lamellar bone; m, muscle; odt, odontoblast; os, osteoid; ost, osteoblast; pd, pedicle; pde, predentin; pg, preganoin; sc, *stratum compactum*; I., anteriorly located scute to the posterior one (II.). [Scale bars: 1 mm (*B–E*), 250 μm (*B*^{i}), 125 μm (*C*^{i}–*E*^{i}), 2 mm (*F–I*), 150 μm (*J–M*), 50 μm (*N–O*), 200 μm (*P*), 100 μm (*Q*), 20 μm (*R–U*).]

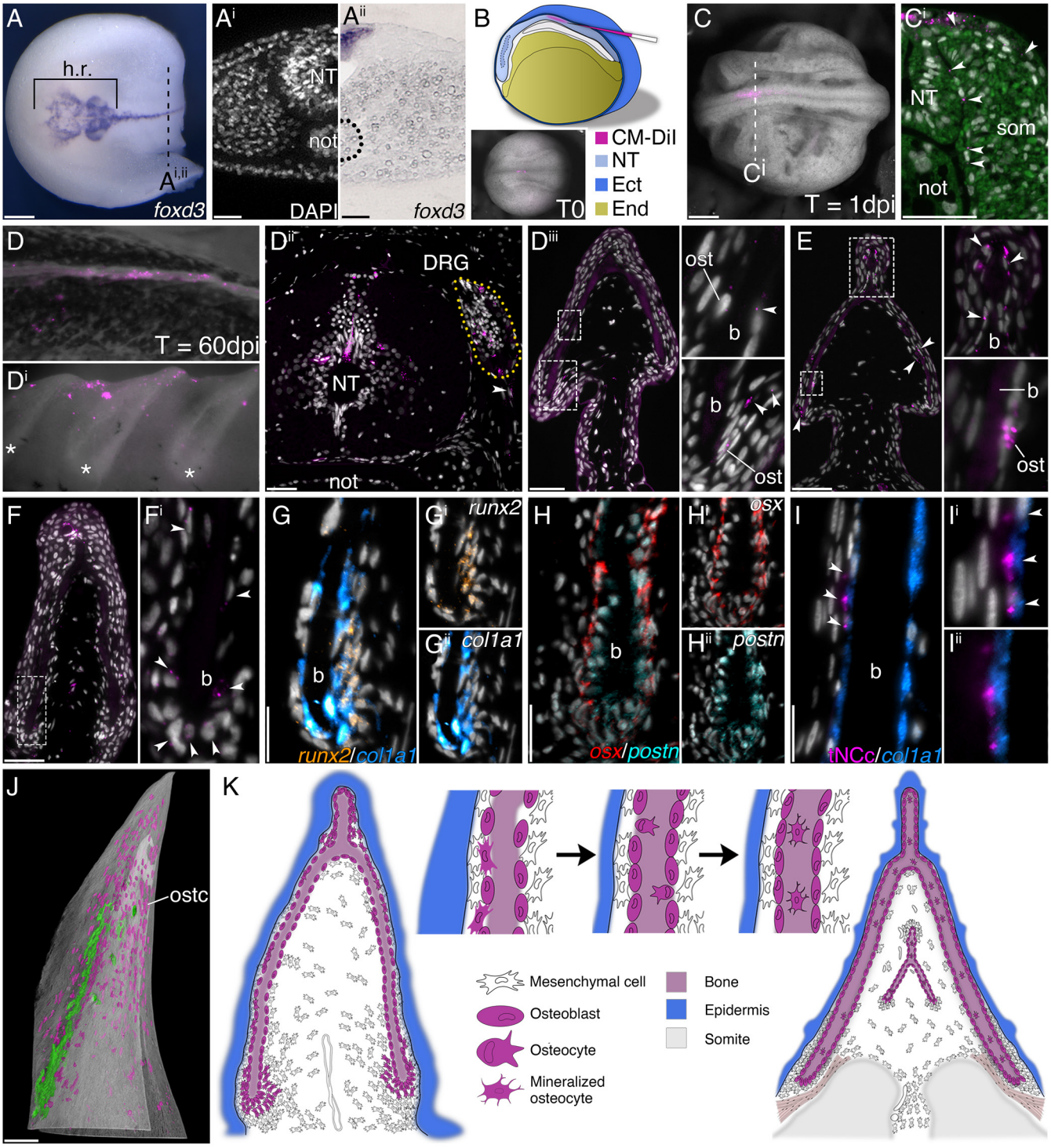

Fig. 2. Trunk neural crest gives rise to osteoblasts of sterlet sturgeon scutes. (*A*) Expression of NC specifier *foxd3* showing premigratory trunk NC cells (A^{ii}) at stage 25, dorsal view. Transverse sections as shown in a through the trunk region (A^{i} and A^{ii}). (*B*) Illustration of CM-DiI microinjections at stage 24 into the lumen (light blue) of the neural tube. Small *Inset* shows an embryo at stage 24 immediately after microinjection. (*C*) CM-DiI-positive trunk NC cells migrating from the dorsal part of the neural tube (NT) at 1 day postinjection (dpi). (C^{i}) Transverse section showing migrating trunk NC cells (white arrowheads) around the somite. (*D* and D^{i}) At 60 dpi, CM-DiI-positive trunk NC cells can be seen in the dorsal scutes (marked by asterisks), dorsal (*D*) and lateral (D^{i}) views. Transverse sections reveal CM-DiI-positive cells within expected NC derivative such as dorsal root ganglia (D^{ii}) (DRG; yellow dotted line). (D^{iii}–F^{i}) Transverse sections show CM-DiI-positive trunk NC cells (white arrowhead) around the bone (b) forming the sterlet scute. *Insets* show higher magnification of CM-DiI-positive cells. (*G*–H^{ii}) HCR against *runx2*, *col1a1*, *osx*, and *postn* (genes associated with osteoblastic differentiation) reveals expression corresponding to the distribution of CM-DiI-positive cells (compare F^{i} and *G*–H^{ii}). (*I*–I^{ii}) Transverse section of sterlet scute shows CM-DiI signals (magenta) overlapping with HCR expression of *col1a1* (early marker of osteoblast; blue). (*J*) microCT reconstruction (for details, see *Material and Methods* and *SI Appendix*, Fig. S5) of osteocytes (magenta) and vascularization (green) within the scute, lateral view. (*K*) Schematic representations suggesting that trunk NC cells give rise to the osteoblasts (ost) and osteocytes (ostc) of the scute. Every letter represents a different experimental animal. h.r., head region; not, notochord. [Scale bars: 500 μm (*A* and *C*), 25 μm (A^{i}, A^{ii}, C^{i}, and *G*–*I*), 50 μm (D^{ii}–*F*), 150 μm (*J*).]

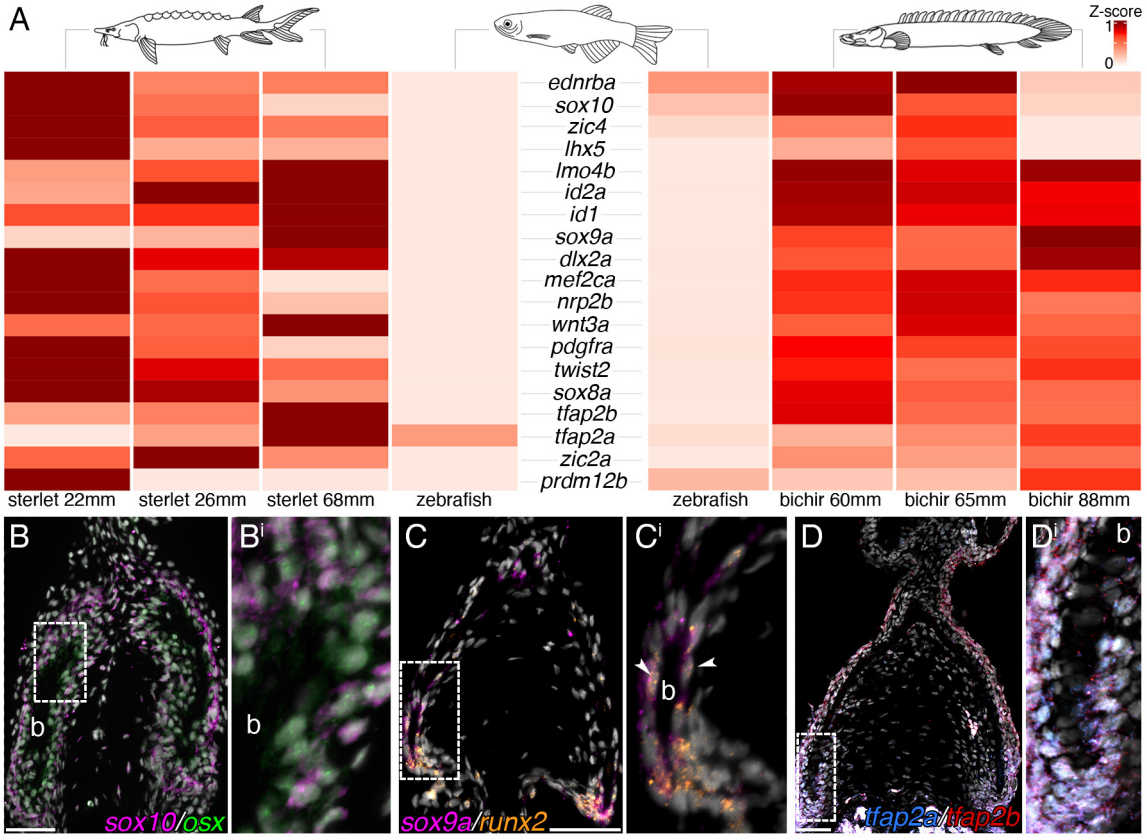

Fig. 3. Scale RNA sequencing comparisons between sterlet, bichir, and zebrafish reveal neural crest GRN gene signature in bichir scales and sterlet scutes. (*A*) Hierarchical clustering analysis focused on genes identified as being part of NC GRN reveals significant enrichment of NC-like genes in sterlet scutes and bichir scales. (*B-D*) Multiplexed fluorescent mRNA in situ hybridizations by HCR reveals expressions of NC-like genes (*sox10*, *sox9a*, *tfpa2a*, and *tfap2b*) and osteoblast markers (*osx* and *runx2*) in sterlet scutes. [Scale bars: 50 μm (*B–D*).]

expression of *runx2* and other genes associated with bone formation such as *osx*, *col1a1,* and *postn* in the scute. The results show that the expression pattern of these skeletal genes corresponds (cf. Fig. 2 *F*, F^{i}, and *G–*H^{ii}) and overlaps with the distribution of CM-DiI-positive cells (Fig. 2 *I–*I^{ii} and *SI Appendix*, Fig. S6 *J–*K^{i}), consistent with the possibility that trunk NC cells give rise to osteoblasts and osteocytes of the scute (Fig. 2 *J* and *K* and *SI Appendix*, Fig. S6). As osteoblasts in teleost scales are exclusively derived from the mesoderm (17–19), we also tested the possible contribution of mesodermal cells to scute development. To this end, we microinjected CM-DiI into the paraxial mesoderm (*SI Appendix*, Fig. S7 *A–*B^{i}). This resulted in labeling cells between the epidermis and the layer of osteoblasts, but not tightly associated with the bone in any of the scutes (n = 19; *SI Appendix*, Fig. S7 C^{iii}*–H*). These findings demonstrate that only the trunk NC gives rise to the osteoblasts that form the bony dermal armor of sterlet sturgeon, as well as a significant contribution to the mesenchymal cells, suggesting an essential role of the trunk NC in the formation of dermal exoskeleton.

NC GRN Gene Signature in Scutes and Scales. To further explore the molecular characteristics of scutes and scales across different fish species, we performed a hierarchical clustering analysis (12) of genes identified as being part of NC GRN (34) in sterlet scutes, bichir ganoid scales, in comparison with zebrafish scales (Fig. 3*A* and *SI Appendix*, Fig. S8 *A–C*). Consistent with our lineage tracing of sterlet trunk NC cells, differential gene expression (DGE) analysis of three developmental stages of sterlet scutes displayed significant enrichment of NC-GRN genes including *sox10*, *tfap2a*, and *tfap2b* (Fig. 3*A* and *SI Appendix*, Fig. S8 *I–*K^{i}). Furthermore, HCR in situ hybridizations support this finding by demonstration of NC-like gene expressions in sterlet scutes (Fig. 3 *B–*D^{i} and *SI Appendix*, Fig. S8 *D–*F^{i}). Similarly, DGE analysis of ganoid scales of the Senegal bichir, which has osteogenic and odontogenic components, identified significantly enriched NC-GRN genes (Fig. 3*A* and *SI Appendix*, Fig. S8) compared to the gene signature analysis of mesoderm-derived zebrafish scales (17–19). Our results indicate that trunk NC possesses ectomesenchymal potential at least in two early branching ray-finned fishes and participates in the development of their dermal exoskeleton. These findings are consistent with the hypothesis that the trunk NC contributed to both odontogenic and osteogenic components of the dermal armor of some vertebrates (10).

Conclusions

It has long been argued that the origin of vertebrate dermal armor is linked to the evolution of neural crest skeletogenic potential (10, 35). The first identifiable dermal armor is attributed to fragments of an enigmatic vertebrate *Anatolepis* from the Late Cambrian to the Early Ordovician (~490 Mya to 450 Mya) (36). It is comprised of tubercles with a central pulp cavity capped by dentin-like tissue; the individual tubercles are connected with a lamellar tissue that may represent a precursor of dermal bone (37) (Fig. 4, *Bottom*). Later ostracoderms and placoderms (jawless and jawed members of the gnathostome stem group) show a definite

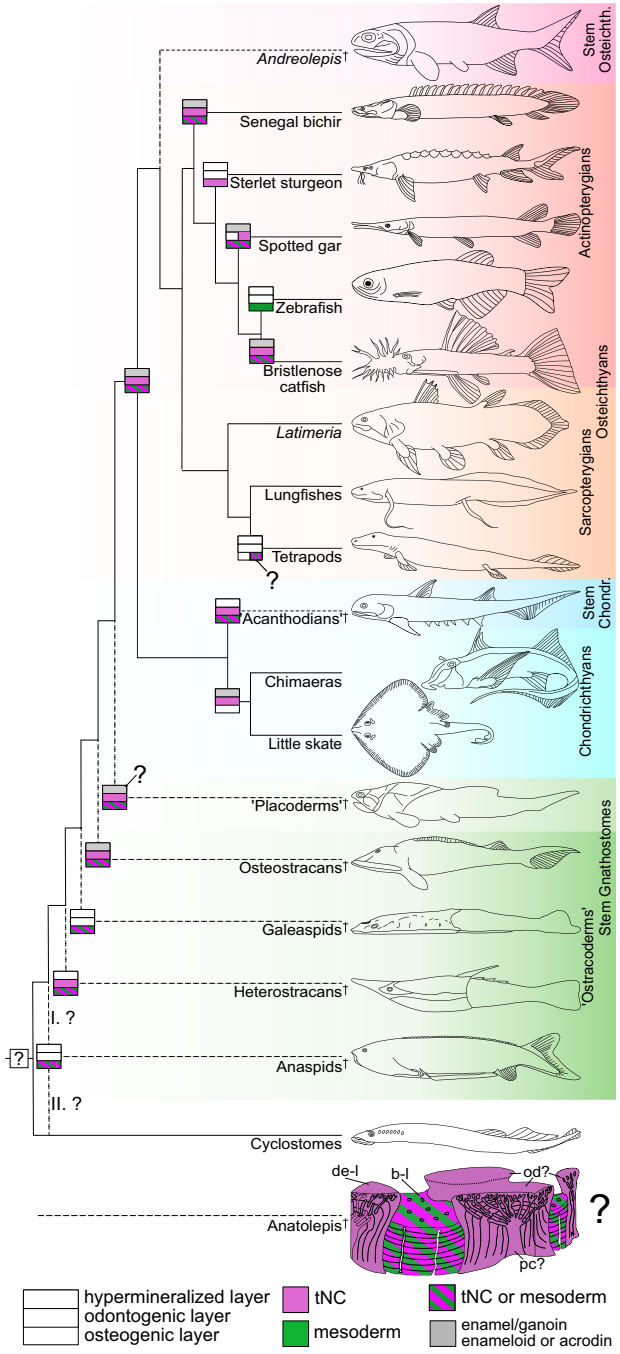

Fig. 4. Trunk NC has the ability to form ectomesenchymal progeny across gnathostomes. Simplified phylogenetic tree of vertebrates, with highlighted extinct lineages (dashed lines) showing composition of dermal armor (rectangle with three units; from top to bottom: hypermineralized, odontogenic, and osteogenic unit) in individual groups of vertebrates. I and II indicate two possible phylogenic positions of anaspids, (I) as a deeply branching ostracoderms (40) or (II) anaspids as stem cyclostomes (41, 42). Based on this, the dermal armor was absent or secondarily lost in the cyclostome lineage (lampreys and hagfishes). Given that the oral and postcranial odontodes in extant gnathostomes seem to be NC derived (13, 43), this strongly implies that the odontogenic unit of dermal armor is trunk NC derived in fossil crown gnathostomes (such as *Andreolepis*) and likely in stem gnathostomes as well. During the rise of tetrapods (lungfishes, porolepiforms, tetrapodomophs) (11), the odontogenic unit was gradually reduced. Indeed, loss of both dermal armor units is apparent in Amniotes (half-filled unites of rectangle). Note trunk NC (magenta)/mesoderm (green) polarity in osteogenic unit contrasting with the exclusively NC-derived odontogenic system. The half-colored box in gar indicates the presence of dentin in denticles. The scheme is based on experimental evidence from zebrafish, little skate, and sterlet sturgeon, for which developmental evidence exist. b-l, bone-like tissue; de-l, dentin-like tissue; od?, possible odontode; pc?, possible pulp cavity.

odontoosteogenic arrangement of dermal armor with reduction or elaboration varying in individual lineages (9, 38, 39) (Fig. 4). Based on lineage tracing of dermal denticles of cartilaginous fishes and highly derived elasmoid scales of teleost fishes, it has been suggested that the odontogenic component of the ancient dermal armor is trunk NC derived, whereas the osteogenic component is mesoderm derived (13).

To understand the evolutionary origin of the ancient dermal armor, we analyzed the dermal exoskeleton of the representatives of all major phylogenetic lineages of ray-finned fishes, including nonteleost groups, such as sturgeons. To directly test the embryonic origin of the osteogenic component of the dermal armor, we took advantage of the accessibility of the sterlet sturgeon, whose scutes completely lack the dentin component. Our data show that trunk NC cells migrate to the developing dorsal scutes where they give rise to osteoblasts comprising the bony elements of the scutes (Fig. 2). This is an unambiguous demonstration of trunk NC forming dermal bone, posterior to the pectoral girdle (44). This is also supported by indirect evidence of gene expression studies in several amniotes (45–47), which inferred that the osteoderms of tetrapod integumentary skeleton may be trunk NC derived as well. For instance, preliminary lineage tracing of late emerging trunk NC in the hard shell turtle suggested the NC origin of the plastron bones (45, 46).

While our results suggest that the postcranial bones can form from trunk NC (cf. Figs. 2 and 4), data from teleost elasmoid scales suggest that the origin of the osteogenic unit was mesodermal (17–19). Three opposing scenarios may explain the origin of sterlet scutes from ancestral ganoid scales (Fig. 4): 1) Trunk NC gave rise to both units, but after reduction of the dentinous portion, trunk NC gave rise to the bony part; or 2) Trunk NC was involved only in the formation of the odontogenic unit; when this unit disappeared, the trunk NC was coopted to make dermal bone; 3) Both NC and mesoderm are equally competent to form bone, such that teleost scales versus sterlet scutes reflect shifts in the contribution of one or the other of these mesenchymal populations in the trunk; a similar situation occurs in the bones of skull vault (48) or pharyngeal endoskeleton (49). We also speculate that the NC/mesoderm origin may correlate with the presence of either a rigid bony plate as in bichir or gar, or an incompletely mineralized elasmodin (plywood-like tissue) as in most teleost scales, respectively. These two types of skeletal tissue (bony versus plywood like) are considered distinct by some authors (50). The origin of the elasmoid scales is still unclear, but it is possible that they have completely lost the thick bony plate typical of ancestral rhomboid scales (8) and evolved a novel tissue produced by a different cell population expressing bone matrix genes (51). This suggests that a mesodermal origin observed in some teleosts may reflect a highly derived condition for elasmoid scales. Further insights into the potential mesodermal origin of plywood-like structures may come from exploring *Latimeria* and lungfish scales. While sterlet scutes are derived as well, the presence of bone is likely a retained primitive character. Thus, we propose that the osteogenic unit of the ancient dermal armor was likely derived from the trunk NC. Together, our results suggest that the trunk NC may have had dentoosteogenic potential along the entire body axis across gnathostomes (Fig. 4), and this ability became restricted to the cranial region only later in tetrapod evolution by spatiotemporal expression changes of some GRN components (12).

Material and Methods

Animal Husbandry. Sterlet sturgeon (*Acipenser ruthenus* Linnaeus, 1758) embryos and larvae were obtained from the Faculty of Fisheries and Protection

of Waters, Research Institute of Fish Culture and Hydrobiology, University of South Bohemia in Ceske Budejovice, Czech Republic. Embryos were held in containers with dechlorinated water at 15 °C until the hatching stage (st. 35). Free-swimming larvae were kept in well-oxygenated containers at 15 to 17 °C until desired developmental stage, and they were euthanized using an overdose of tricaine (1 g/L) prior to fixation in 4% PFA. Sterlet development was staged as previously described by Dettlaff et al. (52). Senegal bichirs (*Polypterus senegalus*, Cuvier 1829) were obtained from the Department of Zoology, Faculty of Science, Charles University in Prague, the Czech Republic, and spotted gars (*Lepisosteus oculatus*, Winchell 1864) from the Department of Integrative Biology, Michigan State University, MI, USA. Fixed bristlenose catfishes (*Ancistrus sp.*) were a generous gift from the personal collection of Mr. Dominik Miler. Individuals were staged based on the total body length (TL). Sterlet embryology work and animal care were approved by the Ministry of Agriculture of the Czech Republic (MSMT-12550/2016-3), followed the principles of the European Union Harmonized Animal Welfare Act of the Czech Republic and Principles of Laboratory Animal Care and National Laws 246/1992 "Animal Welfare," and were conducted in accordance with the Animal Research Committee of RIFCH. The authors of the study own the Certificate of professional competence for designing experiments and experimental projects under Section 15d(3) of the Czech Republic Act no. 246/1992 Coll. on the Protection of Animals against Cruelty. All animal work with bichir was approved by the institutional animal care and use committee of the Charles University in Prague, the Czech Republic. Gar animal work was approved by the IACUC at Michigan State University (protocols 10/16-179-00 and 201900309). Adult zebrafish were maintained in the Beckman Institute Zebrafish Facility at Caltech, and all work was compliant with the animal protocol No. 1764 approved by the IACUC at Caltech.

Cell Lineage Tracing. The sterlet embryos at stage 24 (trunk neural crest) and stage 25 (paraxial mesoderm) were manually removed from the jelly egg membrane and positioned in suitable hollows in modeling clay, allowing proper orientation and stability. Cell tracker CM-DiI (1 mg in 1 mL of 100% ethanol; Thermo Scientific) was diluted (1:5) into 10% sucrose and microinjected through the chorion with injector using microcapillaries (Drummond Microcaps) prepared in a Narishige pc-10 puller (58 °C with two weight elements). After labeling, embryos were kept in the 48-well plates containing E2 zebrafish medium with Pen/Strep antibiotics (120 ng/mL of penicillin and 200 ng/mL of streptomycin) at 15 °C. After hatching, the individuals were maintained in well-oxygenated containers with dechlorinated water in incubators at 15 to 17 °C to the desired developmental stage (22 to 23 mm, approx. 60 d; depending on feeding frequency) and then euthanized using an overdose of tricaine (1 g/L) prior to fixation in 4% PFA. As a control of proper injection, a few embryos were fixed immediately after the injection and analyzed (T0; Fig. 2*B* and *SI Appendix*, Fig. S6 *A* and *A'*). Cell lineage tracing was performed in four independent rounds of injections (always different breeding pairs) during spring 2020 and 2022. To avoid staining of paraxial mesoderm, CM-DiI dye was injected into the lumen of the neural tube (Fig. 2*B* and *SI Appendix*, Fig. S6 *A* and *A'*); thus, only prospective trunk neural crest and dorsal midline of the neural tube were stained. Sixty-six embryos were successfully injected and fixed at stage 24 (n = 7), stage 25 to 26 (n = 10), stage 30 (n = 2), at 15 mm (n = 3), and at 22 to 23 mm (n = 44) (*SI Appendix*, Fig. S6 and Table S1). In the case of paraxial mesoderm fate mapping, the capillary was aimed from above into the paraxial mesoderm which is located laterally to the developing neural tube in sterlet sturgeon embryos; thus, only paraxial mesoderm and nonneural ectoderm were stained. In total, 49 embryos were successfully injected and fixed at stage 25 (n = 10), stage 26 to 27 (n = 20), and at 22 to 23 mm (n = 19) (*SI Appendix*, Fig. S7 and Table S1). To verify that trunk neural crest gives rise to the scute osteoblasts, several specimens with positive CM-DiI signals were used for HCR, but only *col1a1* probe worked properly on 4% PFA fixed samples (trunk NC: n = 6; mesoderm: n = 4; Fig. 2*I* and *SI Appendix*, Fig. S6 *J–K'*). The samples for histological analysis were mounted into JB-4 resin or paraffin (*SI Appendix*, Fig. S7 *F–G*), sectioned (5 μm or 12 μm, respectively), and stained with Fluoroshield with DAPI (Sigma-Aldrich).

HCR. HCR v3.0 was performed according to the protocol suggested by Molecular technologies (53) for zebrafish with several modifications. Briefly, methanol-fixed tissues were rehydrated by series of methanol/PBS-Tween solutions (2 × 100%, 75%, 50%, 25%; every step 15 min), washed in PBS-Tween (2 × 10 min), depigmented by a bleaching mix-solution (formamide, 20× SSC, 30% hydrogen peroxide, and distilled water) under the direct light, washed in PBS-Tween (10 min), treated with proteinase-K for 60 min (22 to 23 mm) or 70 min (26 mm) at room temperature, washed in PBS-Tween (2 × 10 min), postfixed in 4% PFA (10 min), washed in PBS-Tween (2 × 10 min), prehybridized in 30% probe hybridization buffer at 37 °C (60 min), and incubated with probes (usually 2 μL of 1 μM stock per probe mixture) in probe hybridization buffer at 37 °C overnight. HCR on sections (*tfap2b* and *tfap2a*) was performed as described by Criswell and Gillis (54), with the following modifications: cryosections were used instead of paraffin sections, and slides were hybridized overnight at 37 °C with 2 μL of 1 μM probe stock/100 μL of hybridization solution. All probe sets (*sox10*, *sox9a*, *tfap2a*, *tfap2b*, *col1a1*, *osx*, *runx2*), hairpins, and buffers were purchased from Molecular Technologies (https://www.molecularinstruments.com). Each HCR was repeated at least three times with a minimum of three sterlet scutes for each run of HCR (for HCR on sections (Fig. 3*D* and *SI Appendix*, Fig. S8*D*), four slides containing approx. 10 sections from two different specimens were used). HCR on CM-DiI-positive samples followed the same protocol described above, with the following modifications: The individual scute was dissected, depigmentation treatment was skipped, and hybridization was prolonged to 24 h. The samples for histological analysis were mounted into JB-4 resin (described below), sectioned (5 μm), and counterstained with Fluoroshield with DAPI (Sigma-Aldrich). All photographs were taken with Zeiss AxioImager.M2 equipped with an Apotome.2.

Cloning of Sterlet *foxd3* Ortholog and In Situ Hybridization. cDNA was synthesized using SuperScript VILO kit (Invitrogen) and used for the design of PCR amplification primers (*foxd3* : 5′-GAYGTGGAYATCGAYGTGGT-3′; 5′-CTSARRA ARCTVCCGTTGTC-3′). The PCR product was cloned into pGEM-T-Easy vector (Promega) in DH5α-competent *Escherichia coli*. The in situ hybridization protocol is initially similar to HCR, but the samples are prehybridized in the hybridization buffer (50% formamide, 4× SSC, 0.1 mg/mL heparin, 1× Denhardt's, 0.1% CHAPS, 0.2 mg/mL yeast RNA, 10 mM EDTA, 0.1% Tween-20) for at least 120 min. Hybridization was performed at 60 °C with a 1:1,000 dilution of DIG-RNA probe overnight. The next day, the samples were washed at least eight times (each step for 30 min) in wash solution (50% formamide, 4× SSC, 0.1% Tween-20) at 58 °C, then three times in MAB-T (100 mM maleic acid, 150 mM NaCl, 0.1% Tween-20), and blocked in blocking solution (2% blocking reagent, 20% sheep serum in MAB-T) for at least 2 h. Next, the samples were incubated at 4 °C in a blocking solution containing antidigoxigenin antibody (1:3,000; Roche) overnight. The third day, the samples were washed at least eight times (each step for 30 min) in MAB-T and equilibrated in NTMT (0.1 M Tris, 0.1 M NaCl, 0.05 M MgCl2, 0.1% Tween-20). The color reaction was developed in BM-Purple (Roche) until the signal developed. The hybridization was performed at least three times with two embryos per developmental stage, and selected embryos were prepared for vibratome histology as previously described by Stundl et al. (55).

Library Preparation and Sequencing. Samples for RNA-sequencing were preserved in RNAlater (Sigma-Aldrich). For transcriptome sequencing, total RNA was isolated from scales/scutes: bichir (60 mm, 65 mm, 88 mm TL; 10 scales were dissected for each of n = 2 biological replicates); sterlet (22 mm, 26 mm, 68 mm TL; 2 scutes were dissected for each of n = 2 biological replicates); and zebrafish (~3 cm TL; 15 scales were dissected for each of n = 2 biological replicates) using the RNAqueous kit (Ambion) and assessed using the Agilent Bioanalyzer. The RNA-sequencing was performed at the Millard and Muriel Jacobs Genetics and Genomics Laboratory (California Institute of Technology, Pasadena, CA, USA) at 50 million, 50 bp, single-ended reads on two biological replicates for all the three species. The libraries were built according to Illumina Standard Protocols. SR50 sequencing was performed in an HiSeq2500 Illumina sequencer.

Proteome Alignment and Statistical Analysis of Sterlet, Bichir, and Zebrafish Scute and Scale RNA-seq Datasets. To identify orthologous genes between sterlet sturgeon, Senegal bichir, and zebrafish, we followed the methods described by Martik et al. (12), with minor modifications. Sterlet sturgeon (genome assembly ASM1064508v1)/Senegal bichir (genome assembly ASM1683550v1) proteome obtained from NCBI was aligned to the zebrafish (genome assembly GRCz11) proteome using the BLAST alignment software available on the UCSC genome browser (56). In brief, every sterlet/bichir protein sequence was queried locally against the zebrafish proteome, following which regions with the longest alignment were matched to the respective zebrafish proteins. Using this alignment-based approach,

proteins with highest alignment percentage score (Dataset S1; Dataset S2 for exact scores for each ortholog) were identified as orthologs. Sterlet/bichir scute/scale RNA sequencing libraries were aligned to the sterlet/bichir sequences, while the zebrafish scale RNA sequencing libraries were aligned to the zebrafish sequences using Bowtie2 (57). Transcript counts were calculated using featureCounts (58), and DGE analysis was performed using DESeq2 (59). Using zebrafish gene annotations as a reference, we added the transcript counts for duplicated orthologs found in the sterlet/bichir genome to calculate an "aggregated" transcript count for each gene as described by Martik et al. (12). These aggregated transcript counts were then normalized using the formula: $Z_i = T_i - \min(T)/\max(T) - \min(T)$ where Z_i is the normalized transcript count and T_i is the absolute transcript count. A subset of genes previously identified as being part of the neural crest gene regulatory network (34) was then isolated from the count matrix and plotted as a heatmap using *ComplexHeatmap* (60) package in Rstudio. The sterlet has a paralog retention rate of about 70% from its genome duplication; thus, all IDs of candidate genes were used for further analysis, and paralogs (*SI Appendix*, Table S2) were phylogenetically analyzed (amino acid tree made using the maximum likelihood method [PhyML 3.0 (61) http://www.atgc-montpellier.fr/phyml/] on a Clustal Omega 1.2.3 alignment, bootstrap score n = 100).

X-Ray Microtomography (microCT). Specimens for microCT were dissected and mounted without contrast staining (62) and scanned with an MicroXCT-200 (Zeiss/Xradia, Germany) at the Department of Evolutionary Biology, Theoretical Biology Unit, University of Vienna. The scans were acquired from bichir scale (20 cm TL; 1.0 μm voxel size), sterlet dorsal scute (68 mm TL; 2.5 μm voxel size), gar scale (125 mm TL; 1.0 μm voxel size), and armored catfish scute (35 mm TL; 1.0 μm voxel size). 3D modeling from the virtual thin sections was segmented in the software VG Studio 3.4 at the Department of Organismal Biology of Uppsala University, Sweden.

Histology. Visualization of mineralized tissues was carried out as described previously (63). All photographs were taken in numerous focal planes with Olympus MVX10 stereoscope with AxioCam and the final images were prepared with Helicon Focus Pro (HeliconSoft), allowing to form high-resolution images. Mineralized tissues for histological analysis were washed in distilled water and placed in Morse's solution (10% sodium citrate and 22.5% formic acid) at room temperature for decalcification until the tissues were soft. Next, the samples were dehydrated in 100% ethanol and incubated in an infiltration solution of JB-4 resin (prepared according to the manufacturer's instructions; Sigma-Aldrich) at room temperature overnight. The next day, the infiltration solution was replaced by an embedding solution (prepared according to the manufacturer's instructions), placed into an embedding mold (PolyScience), and transferred to a vacuum chamber which accelerated the polymerization (~3 h). The resin block was sectioned at 5 μm, and sections were stained with Mayer's hematoxylin (except *SI Appendix*, Fig. S2*I*) or Verde Luz-orange G-acid fuchsin (VOF) stain (*SI Appendix*, Fig. S2*I*).

Data, Materials, and Software Availability. The RNA-seq data reported in this paper have been deposited in the National Center for Biotechnology Information Gene Expression Omnibus database (accession no. GSE235280) (64).

ACKNOWLEDGMENTS. We would like to thank Igor Adameyko for his helpful comments. We also thank Michaela Fučíková, David Gela, Martin Kahanec, and Marek Rodina for the sterlet spawns; David Mayorga and Ryan Fraser for zebrafish care; Brett Raciot for spotted gar care; Johanna Tan-Cabugao and Constanza Gonzales for technical assistance; Dominik Miler for the generous gift of catfish individuals; the Caltech Millard and Muriel Jacobs Genetics and Genomics Laboratory and in particular Vijaya Kumar and Igor Antoshechkin for preparation and sequencing of our RNA-seq libraries. We would also like to thank all our fishes for providing embryonic material for our research. The project has received funding from the European Union's Horizon 2020 research and innovation program under Marie Sklodowska-Curie grant agreement No. 897949 (to J.S.) and from National Institutes of Health grant R35NS111564 to (M.E.B). D.C. and P.E.A. were supported by a Wallenberg Scholarship from the Knut & Alice Wallenberg Foundation, awarded to P.E.A. M.L.M. was supported by a fellowship from the Helen Hay Whitney Foundation and by NIH grant 1K99HD100587. J.S., R.F., and M.P. were supported by the Ministry of Education, Youth and Sports of the Czech Republic–project Biodiversity (CZ.02.1.01/0.0/0.0/16_025/0007370) and the Czech Science Foundation (No. 20-23836S). R.C. was supported by the Czech Science Foundation (No. 19-18634S). Gar work in the Braasch Lab is supported by NSF EDGE FGT grant #2029216.

Author affiliations: [a]Division of Biology and Biological Engineering, California Institute of Technology, Pasadena, CA 91125; [b]Faculty of Fisheries and Protection of Waters, University of South Bohemia in Ceske Budejovice, 38925 Vodnany, Czech Republic; [c]Department of Organismal Biology, Uppsala University, SE-75236 Uppsala, Sweden; [d]Department of Zoology, Faculty of Science, Charles University in Prague, 128 00 Prague, Czech Republic; [e]Department of Evolutionary Biology, Theoretical Biology Unit, University of Vienna, 1010 Vienna, Austria; [f]Department of Integrative Biology, Michigan State University, East Lansing, MI 48824; and [g]Ecology, Evolution and Behavior Program, Michigan State University, East Lansing, MI 48824

1. N. M. Le Douarin, *The Neural Crest* (Cambridge University Press, 1982).
2. C. Gans, R. G. Northcutt, Neural crest and the origin of vertebrates: A new head. *Science* **220**, 268–274 (1983).
3. B. K. Hall, *The Neural Crest and Neural Crest Cells in Vertebrate Development and Evolution* (Springer, US, 2009).
4. M. Simoes-Costa, M. E. Bronner, Reprogramming of avian neural crest axial identity and cell fate. *Science* **352**, 1570–1573 (2016).
5. I. M. McGonnell, A. Graham, Trunk neural crest has skeletogenic potential. *Curr. Biol.* **12**, 767–771 (2002).
6. A. G. Lumsden, Spatial organization of the epithelium and the role of neural crest cells in the initiation of the mammalian tooth germ. *Development* **103**, 155–169 (1988).
7. R. Soldatov *et al.*, Spatiotemporal structure of cell fate decisions in murine neural crest. *Science* **364**, eaas9636 (2019).
8. J.-Y. Sire, P. C. J. Donoghue, M. K. Vickaryous, Origin and evolution of the integumentary skeleton in non-tetrapod vertebrates. *J. Anat.* **214**, 409–440 (2009).
9. M. Rocha *et al.*, From head to tail: Regionalization of the neural crest. *Development* **147**, dev193888 (2020).
10. M. M. Smith, B. K. Hall, A developmental model for evolution of the vertebrate exoskeleton and teeth in *Evolutionary Biology*, M. K. Hecht, R. J. MacIntyre, M. T. Clegg, Eds. (Springer US, 1993), **vol. 27**, pp. 387–448.
11. M. K. Vickaryous, J.-Y. Sire, The integumentary skeleton of tetrapods: Origin, evolution, and development. *J. Anat.* **214**, 441–464 (2009).
12. M. L. Martik *et al.*, Evolution of the new head by gradual acquisition of neural crest regulatory circuits. *Nature* **574**, 675–678 (2019).
13. J. A. Gillis, E. C. Alsema, K. E. Criswell, Trunk neural crest origin of dermal denticles in a cartilaginous fish. *Proc. Natl. Acad. Sci. U.S.A.* **114**, 13200–13205 (2017).
14. J. Jing *et al.*, Spatiotemporal single-cell regulatory atlas reveals neural crest lineage diversification and cellular function during tooth morphogenesis. *Nat. Commun.* **13**, 4803 (2022).
15. M. M. Smith, B. K. Hall, Development and evolutionary origins of vertebrate skeletogenic and odontogenic tissues. *Biol. Rev.* **65**, 277–373 (1990).
16. J. N. Keating, C. L. Marquart, P. C. Donoghue, Histology of the heterostracan dermal skeleton: Insight into the origin of the vertebrate mineralised skeleton. *J. Morphol.* **276**, 657–680 (2015).
17. A. Shimada *et al.*, Trunk exoskeleton in teleosts is mesodermal in origin. *Nat. Commun.* **4**, 1638–1639 (2013).
18. A. Mongera, C. Nüsslein-Volhard, Scales of fish arise from mesoderm. *Curr. Biol.* **23**, R338–R339 (2013).
19. R. T. H. Lee, J. P. Thiery, T. J. Carney, Dermal fin rays and scales derive from mesoderm, not neural crest. *Curr. Biol.* **23**, R336–R337 (2013).
20. M. Smith *et al.*, Trunk neural crest origin of caudal fin mesenchyme in the zebrafish *Brachydanio rerio*. *Proc. Biol. Sci.* **256**, 137–145 (1994).
21. E. Kague *et al.*, Skeletogenic fate of zebrafish cranial and trunk neural crest. *PLoS One* **7**, 1–13 (2012).
22. E. J. Hilton, L. Grande, Review of the fossil record of sturgeons, family Acipenseridae (Actinopterygii: Acipenseriformes), from North America. *J. Paleontol.* **80**, 672–680 (2006).
23. M. Alison *et al.*, Paddlefish and sturgeon (Chondrostei: Acipenseriformes: Polyodontidae and Acipenseridae) from lower Paleocene deposits of Montana, U.S.A. *J. Vertebr. Paleontol.* **40**, 2 (2020).
24. A. N. Sewertzoff, The development of the scales of Acipenser ruthenus. *J. Morphol.* **42**, 523–560 (1926).
25. W. E. Bemis, E. K. Findeis, L. Grande, An overview of Acipenseriformes. *Environ. Biol. Fishes* **48**, 25–71 (1997).
26. Q. Qu *et al.*, New genomic and fossil data illuminate the origin of enamel. *Nature* **526**, 108–111 (2015).
27. O. Hertwig, Ueber das Hautskelet der Fische. 2: Das Hautskelet der Ganoiden (Lepidosteus und Polypterus). *Morphol. Jahrb.* **5**, 1–21 (1879).
28. T. Kerr, The scales of primitive living actinopterygians. *Proc. Zool. Soc. Lond.* **122**, 55–78 (1952).
29. J.-Y. Sire, Scales in young Polypterus senegalus are elasmoid: new phylogenetic implications. *Am. J. Anat.* **186**, 315–323 (1989).
30. J.-Y. Sire, Light and TEM study of nonregenerated and experimentally regenerated scales of Lepisosteus oculatus (Holostei) with particular attention to ganoine formation. *Anat. Rec.* **240**, 189–207 (1994).
31. S. Mori, T. Nakamura, Redeployment of odontode gene regulatory network underlies dermal denticle formation and evolution in suckermouth armored catfish. *Sci. Rep.* **12**, 6172 (2022).
32. Z. Liu *et al.*, The channel catfish genome sequence provides insights into the evolution of scale formation in teleosts. *Nat. Commun.* **7**, 11757 (2016).

33. C. J. Rivera-Rivera, J. I. Montoya-Burgos, Trunk dental tissue evolved independently from underlying dermal bony plates but is associated with surface bones in living odontode-bearing catfish. *Proc. Biol. Sci.* **284**, 20171831 (2017).
34. M. L. Martik, M. E. Bronner, Regulatory logic underlying diversification of the neural crest. *Trends Genet.* **33**, 715–727 (2017).
35. M. M. Smith, Putative skeletal neural crest cells in early late ordovician vertebrates from colorado. *Science* **251**, 301–303 (1991).
36. J. E. Repetski, A fish from the Upper Cambrian of North America. *Science* **200**, 529–531 (1978).
37. M. P. Smith, I. J. Sansom, E. J. Repetski, Histology of the first fish. *Science* **380**, 702–704 (1996).
38. S. Giles, M. Rücklin, P. C. J. Donoghue, Histology of 'placoderm' dermal skeletons: Implications for the nature of the ancestral gnathostome. *J. Morphol.* **274**, 627–644 (2013).
39. J. N. Keating, P. C. J. Donoghue, Histology and affinity of anaspids, and the early evolution of the vertebrate dermal skeleton. *Proc. Biol. Sci.* **283**, 20152917 (2016).
40. P. Janvier, Facts and fancies about early fossil chordates and vertebrates. *Nature* **520**, 483–489 (2015).
41. T. Miyashita *et al.*, Hagfish from the Cretaceous Tethys Sea and a reconciliation of the morphological-molecular conflict in early vertebrate phylogeny. *Proc. Natl. Acad. Sci. U.S.A.* **116**, 2146–2151 (2019).
42. T. Miyashita *et al.*, Non-ammocoete larvae of Paleozoic stem lampreys. *Nature* **591**, 408–412 (2021).
43. Y. Chai *et al.*, Fate of the mammalian cranial neural crest during tooth and mandibular morphogenesis. *Development* **127**, 1671–1679 (2000).
44. T. Matsuoka *et al.*, Neural crest origins of the neck and shoulder. *Nature* **436**, 347–355 (2005).
45. J. A. Cebra-Thomas *et al.*, Evidence that a late-emerging population of trunk neural crest cells forms the plastron bones in the turtle Trachemys scripta. *Evol. Dev.* **9**, 267–277 (2007).
46. J. A. Cebra-Thomas *et al.*, Late-emigrating trunk neural crest cells in turtle embryos generate an osteogenic ectomesenchyme in the plastron. *Dev. Dyn.* **242**, 1223–1235 (2013).
47. C. M. Krmpotic *et al.*, The dorsal integument of the Southern Long-nosed armadillo Dasypus hybridus (Cingulata, Xenarthra), and a possible neural crest origin of the osteoderms. Discussing evolutive consequences for Amniota. *J. Mamm. Evol.* **28**, 635–645 (2021).
48. C. S. Teng *et al.*, Resolving homology in the face of shifting germ layer origins: Lessons from a major skull vault boundary. *eLife* **8**, e52814 (2019).
49. V. A. Sleight, J. A. Gillis, Embryonic origin and serial homology of gill arches and paired fins in the skate, Leucoraja erinacea. *eLife* **9**, e60635 (2020).
50. J.-Y. Sire, M.-A. Akimenko, Scale development in fish: A review, with description of sonic hedgehog (shh) expression in the zebrafish (Danio rerio). *Int. J. Dev. Biol.* **48**, 233–247 (2004).
51. I. Adameyko, Elaboration of fates in neural crest lineage during evolution in *Evolving Neural Crest Cells*, B. F. Eames, D. Medeiros, I. Adameyko, Eds. (CRC Press, Boca Raton, 2020), pp. 157–183
52. T. A. Dettlaff, A. S. Ginsburg, O. I. Schmalhausen, *Sturgeon Fishes: Developmental Biology and Aquaculture* (Springer Verlag, 1993).
53. H. M. T. Choi *et al.*, Third-generation in situ hybridization chain reaction: Multiplexed, quantitative, sensitive, versatile, robust. *Development* **145**, 1–10 (2018).
54. K. E. Criswell, A. J. Gillis, Resegmentation is an ancestral feature of the gnathostome vertebral skeleton. *eLife* **9**, e51696 (2020).
55. J. Stundl *et al.*, Migratory patterns and evolutionary plasticity of cranial neural crest cells in ray-finned fishes. *Dev. Biol.* **467**, 14–29 (2020).
56. D. Karolchik *et al.*, The UCSC genome browser database. *Nucleic Acids Res.* **31**, 51–54 (2003).
57. B. Langmead, S. Salzburg, Fast gapped-read alignment with Bowtie 2. *Nat. Methods* **9**, 357–359 (2012).
58. Y. Liao, G. K. Smyth, W. Shi, featureCounts: An efficient general purpose program for assigning sequence reads to genomic features. *Bioinformatics* **30**, 923–930 (2014).
59. M. I. Love, W. Huber, S. Anders, Moderated estimation of fold change and dispersion for RNA-seq data with DESeq2. *Genome Biol.* **15**, 550 (2014).
60. Z. Gu, R. Eils, M. Schlesner, Complex heatmaps reveal patterns and correlations in multidimensional genomic data. *Bioinformatics* **32**, 2847–2849 (2016). 10.1093/bioinformatics/btw313.
61. S. Guindon *et al.*, New algorithms and methods to estimate maximum-likelihood phylogenies: Assessing the performance of PhyML 3.0. *Syst. Biol.* **59**, 307–321 (2010).
62. B. D. Metscher, MicroCT for developmental biology: A versatile tool for high-contrast 3D imaging at histological resolutions. *Dev. Dyn.* **238**, 632–640 (2009).
63. M. H. Connolly, P. C. Yelick, High-throughput methods for visualizing the teleost skeleton: Capturing autofluorescence of alizarin red. *J. Appl. Ichthyol.* **26**, 274–277 (2010).
64. J. Stundl *et al.*, Ancient vertebrate dermal armor evolved from trunk neural crest. NCBI Gene Expression Omnibus. https://www.ncbi.nlm.nih.gov/geo/query/acc.cgi?acc=GSE235280. Deposited 24 June 2023.

PNAS

Supporting Information for

Ancient vertebrate dermal armor evolved from trunk neural crest

Jan Stundl*, Megan L. Martik, Donglei Chen, Ayyappa D. Raja, Roman Franěk, Anna Pospisilova, Martin Pšenička, Brian D. Metscher, Ingo Braasch, Tatjana Haitina, Robert Cerny, Per E. Ahlberg, Marianne E. Bronner*

Marianne E. Bronner & Jan Stundl
Email: mbronner@caltech.edu & jstundl@caltech.edu

This PDF file includes:

Figures S1 to S8
Tables S1 to S2
Legends for Movies S1 to S4
Legends for Datasets S1 to S2

Other supporting materials for this manuscript include the following:

Movies S1 to S4
Datasets S1 to S2

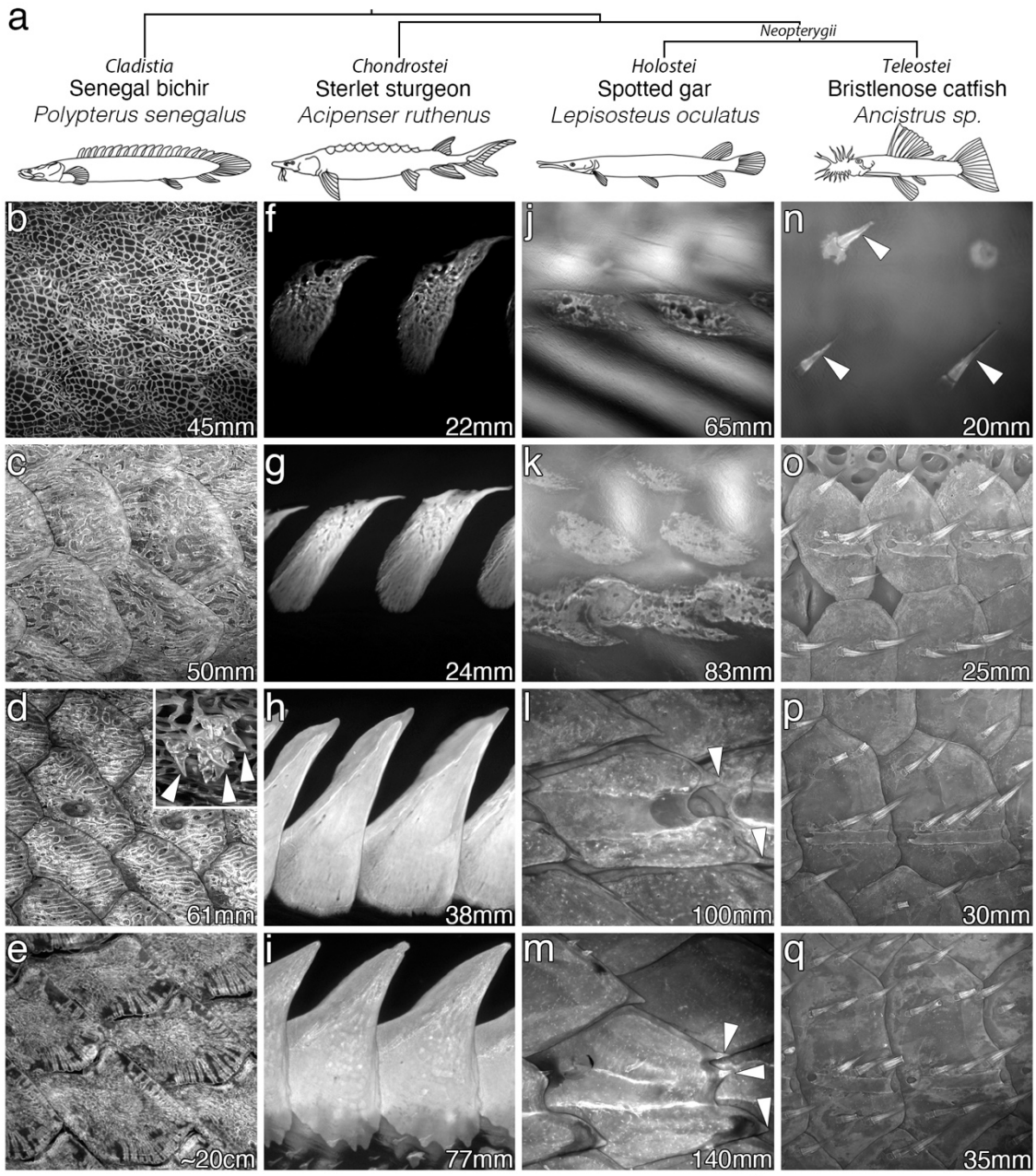

Fig. S1. Comparison of scales and scutes development in studied species. **a**, Simplified phylogeny of ray-finned fishes highlighting studied species. **b-q**, Alizarin Red showing lateral views on developing scales and scutes at different sizes of animals. White arrowheads mark the superficial denticles.

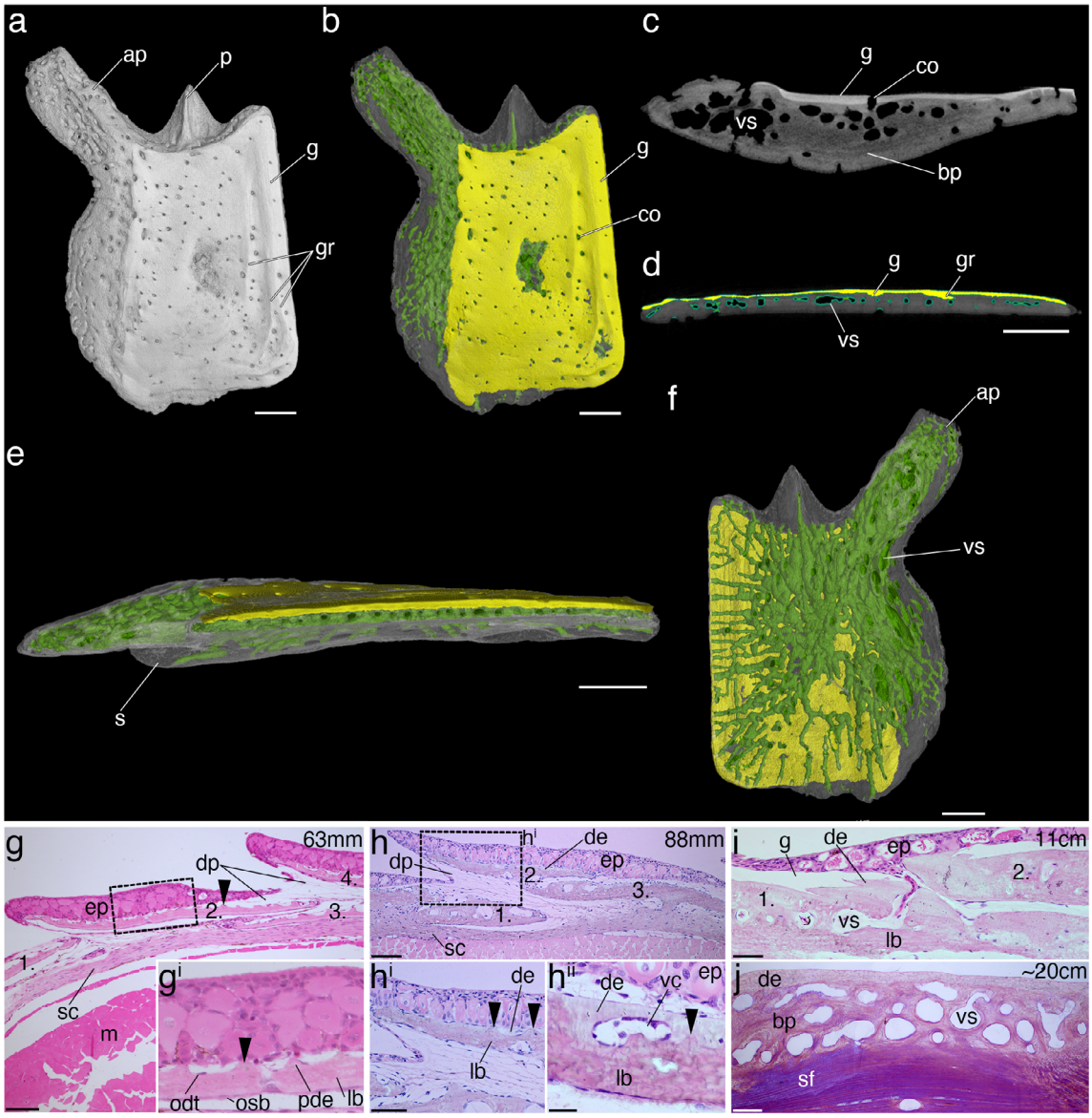

Fig. S2. Bichir ganoid scales. **a**, An overview of bichir scale (~ 20cm), modeled from microCT scan. **b**, Transparent rendering of a, showing the ganoin layer (yellow) and vascularization (green). **c-d**, Virtual sections from the scan dataset. **a-b**, external view; **e**, ventral view; **f**, internal view. **g-j**, Transverse sections showing morphogenesis of bichir scales at three different sizes. Black arrowheads mark the ornamented outer layer of the scale. White arrowheads mark osteocytes. ap, anterior process; bp, bony plate; co, canal openings; ep, epidermis; de, dentin; dp, dermal pockets; g, ganoin; gr, growth increments of ganoin; iel, inner epithelial layer; lb, lamelar bone; m, muscle; odt, odontoblast; osb, osteoblast; p, peg; pde, predentin; pg, preganoin; s, socket; sc, *stratum compactum*; sf, Sharpey's fibers; vc, vascular canal.

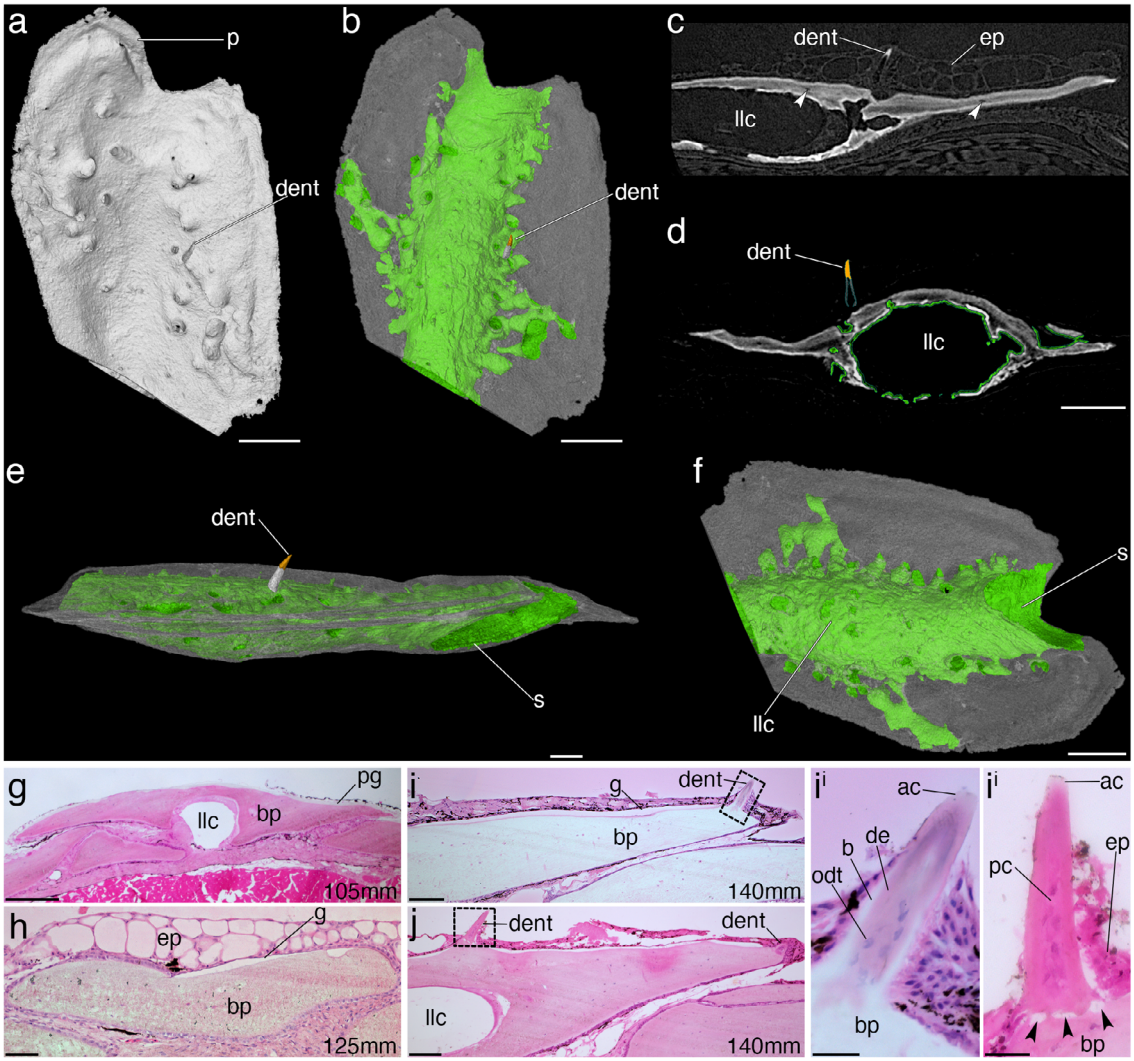

Fig. S3. Gar ganoid scales. **a**, An overview of gar scale (125 mm) in dorsal view, modeled from microCT scan. **b**, Transparent rendering of a, showing vascularization (green) and acrodin cap (ac; yellow) of the single denticle (dent). **c-d**, Virtual sections from the scan dataset. **a-b**, external view; **e**, ventral view; **f**, internal view. **g-i**^{i}, Transverse sections showing morphogenesis of gar ganoid scales at two different sizes. Black arrowheads mark pediments. White arrowheads mark osteocytes. bp, bony plate; de, dentin; ep, epidermis; g, ganoin; llc, lateral line canal; odt, odontoblast; p, peg; pc, pulp cavity; pg, preganoin; s, socket.

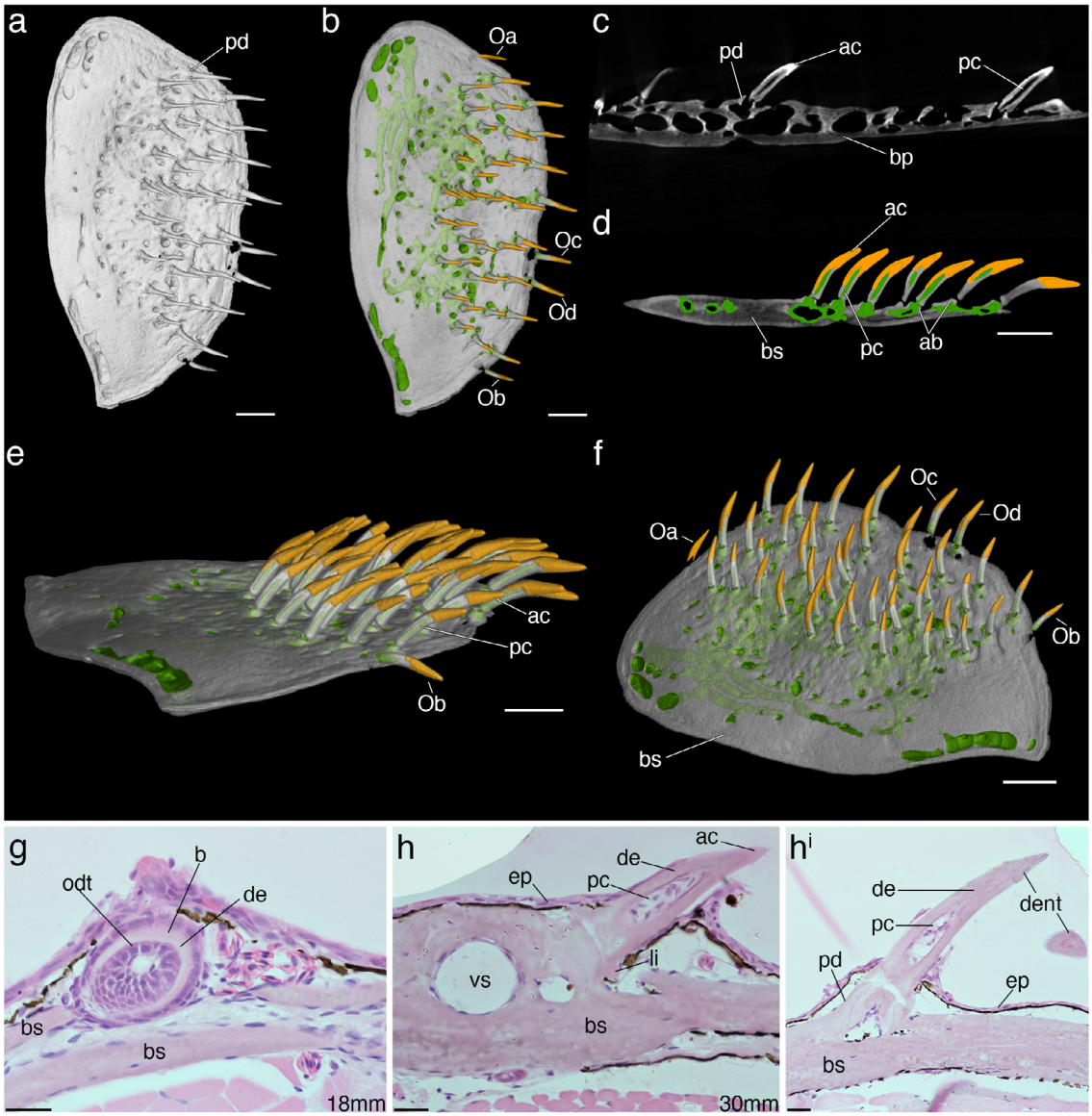

Fig. S4. Scute of bristlenose catfish. **a**, An overview of catfish scute (35 mm) in dorsal view, modeled from microCT scan. **b**, Transparent rendering of a, showing vascularization (vs; green) and modeled acrodin cap (ac; gold) of several superficial denticles. **c-d**, Virtual sections from the scan dataset. Modeled structures (acrodin, vascularization) are highlighted in colors in **d**. **a-b**, external view; **e**, ventral view; **f**, ventroexternal view. Primary denticles are added at the posterior edge of the scute: the acrodin cap that points posteriorly but extends antero-basaly as a ridge is deposited before dentin (Oa); the dentin cone is produced when the crown is still lying flat beneath the epidermis (Ob); the denticle is rotated upright before attachment (Oc); a bony pedicle is formed to anchor the denticle to the supporting bone, with ligaments linking mainly at the anterior side of the denticle base (Od). **g-h**^{i}, Transverse sections showing morphogenesis of catfish scutes at two different sizes. ab, attachment bone; bp, bony plate; bs, bony scute; de, dentin; ep, epidermis; li, ligament; pc, pulp cavity; pd, pedicle; pg, preganoin; s, socket; sc, *stratum compactum*.

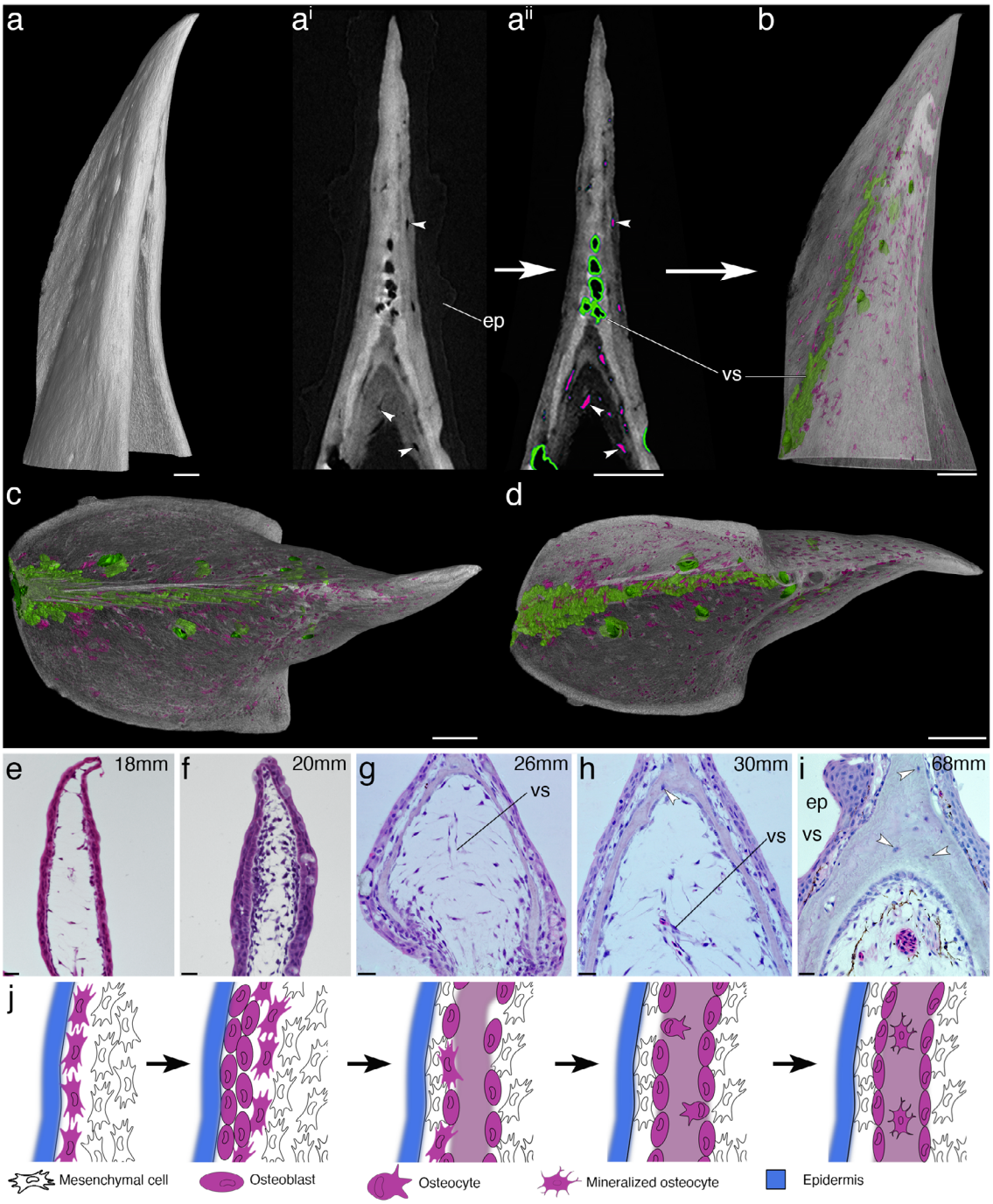

Fig. S5. Sterlet sturgeon scutes. **a**, An overview of sterlet scute (68mm) in lateral view, modeled from microCT scan. **a^{i}-a^{ii}**, Virtual sections from the scan dataset. a^{ii} modeled structures are highlighted in colors: osteocytes (magenta), vascularization (green). **b-d**, Transparent rendering of the model. **b**, lateral view; **c**, dorsal view; **d**, ventrolateral view. **e-i**, Transverse sections show the process of osteogenesis during scute morphogenesis. **j**, Schematic of osteogenesis where individual stages correspond to transverse sections (e-i). White arrowheads mark osteocytes. ep, epidermis; vs, vascularization.

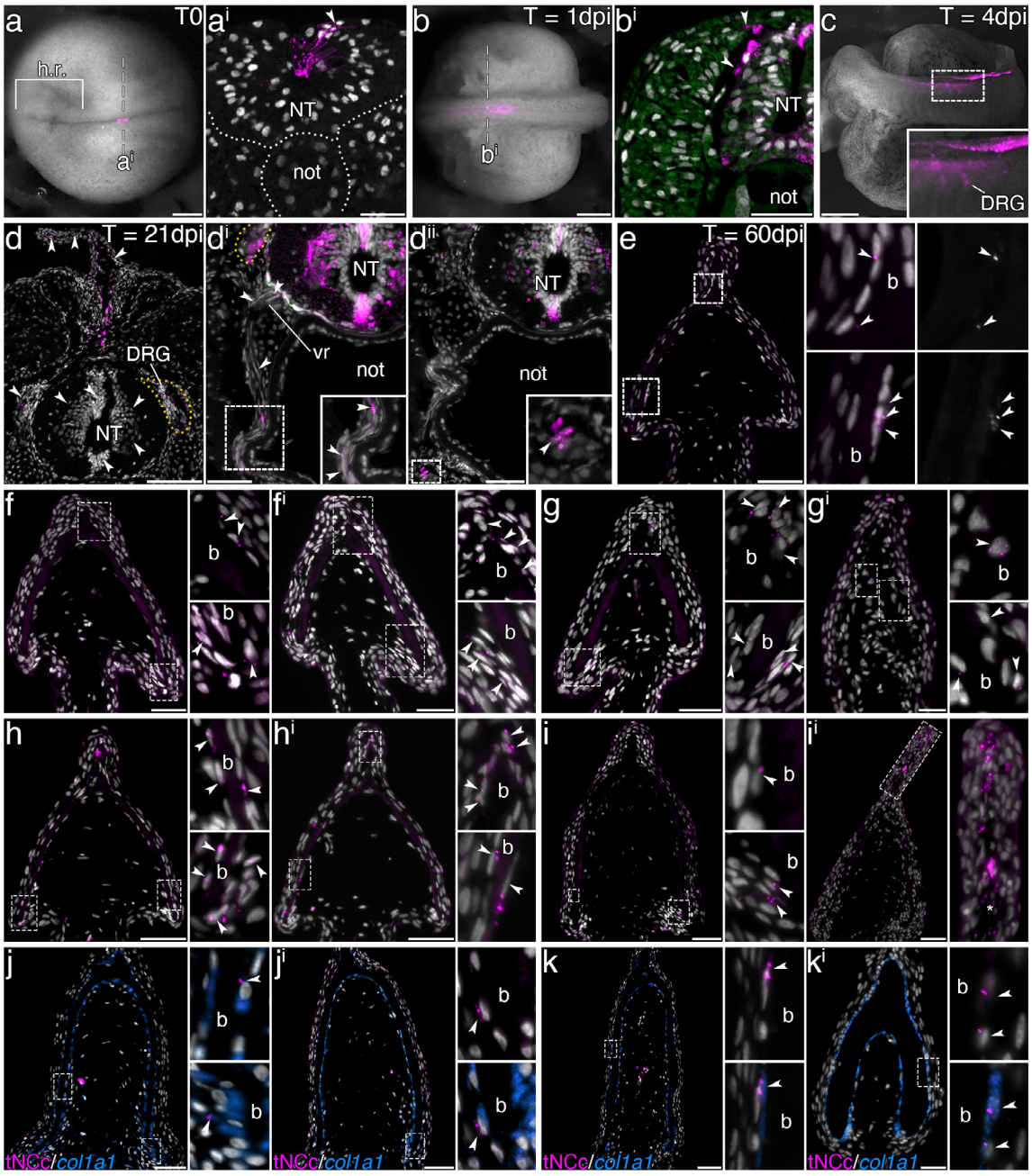

Fig. S6. Trunk neural crest migration and differentiation into the osteoblasts of sterlet. **a**, Embryo at stage 24 immediately after microinjections. **a**^{i}, Transverse section indicated in **a**, showing CM-DiI signals in the neural ectoderm of the forming neural tube (white arrowhead) and lumen of the neural tube. **b**, CM-DiI-positive trunk NC cells migrating from the dorsal part of the neural tube (NT) at one day post-injection (dpi). **b**^{i}, Transverse section indicated in **b**, showing migrating trunk NC cells (white arrowheads) around the somite. **c**, After four days post-injection, the trunk NC migrate into the forming dorsal "fin fold". Small inset shows positive signals in dorsal root ganglia (DRG). **d-d**^{ii}, Transverse sections showing trunk NC cells (white arrowheads) migration to the dorsal "fin fold" (d), migration along the axon bundles (d^{i}) and contribution of trunk NC to DRG (d), and sympathetic ganglia (d^{ii}). **e-i**^{i}, Transverse sections show CM-DiI-positive trunk NC cells (white arrowheads) around the bone (b) forming in the sterlet scute. Insets show higher magnification of CM-DiI-positive cells (insets in e show CM-DiI signals without DAPI). **j-k**^{i}, Transverse sections of sterlet scute show CM-DiI signals (magenta) overlapping with HCR expression of *col1a1* (early

marker of osteoblast; blue). Every letter represents a different experimental animal. h.r., head region; not, notochord. Scale bars: 500 μm (a-c), 50 μm (b^i, d^i-k^i), 25 μm (a^i), 100 μm (d).

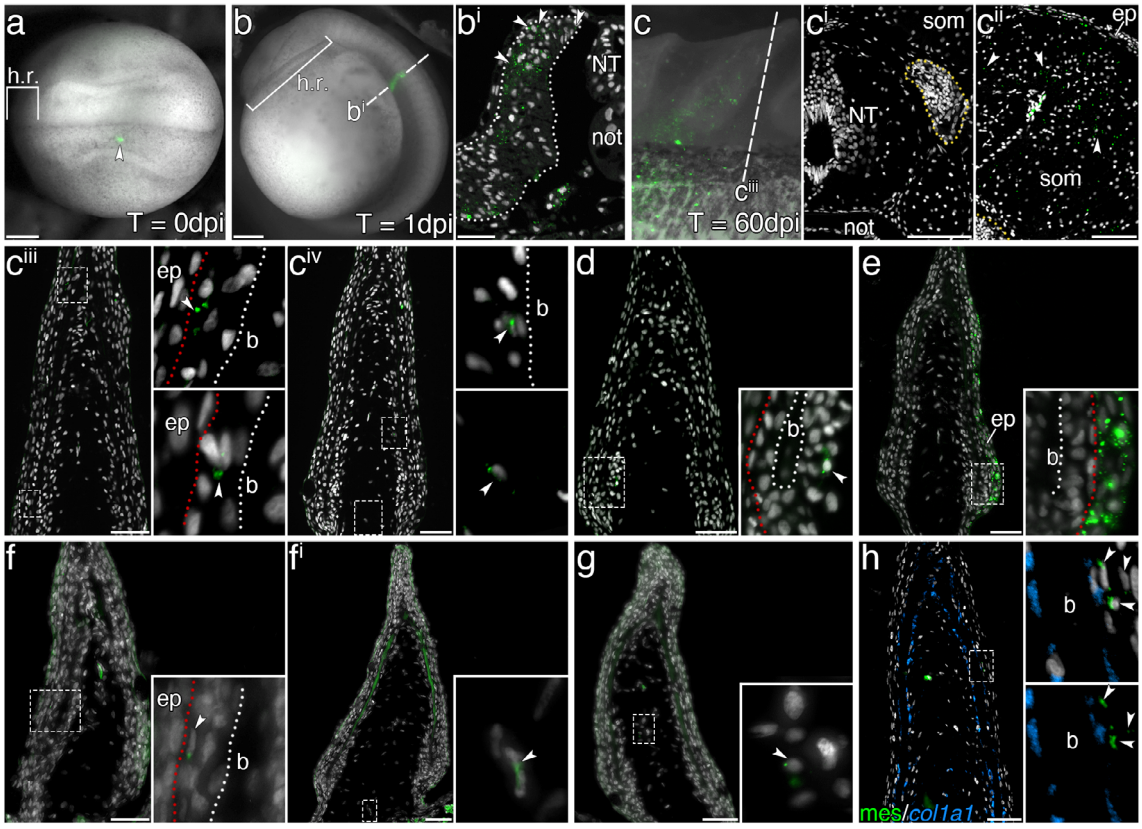

Fig. S7. Paraxial mesoderm does not give rise to the scute osteoblasts. **a**, Paraxial mesoderm was microinjected at stage 25, dorsal view. **b**, Embryo one day post-injection (dpi) showing CM-DiI signals in differentiating somite (**b**^{i}; transverse section indicated in b; white arrowheads mark CM-DiI signal in the dorsal part of the somite, which produces migratory dermomyotomal cells). **c**, At 60 dpi, CM-DiI-positive cells are visible in the dorsal scute (see also c^{iii-iv}). Transverse sections show no CM-DiI-positive cells within the neural tube (NT) or dorsal root ganglia (DRG; yellow dotted line) (c^{i}). The CM-DiI-positive cells are observed within the trunk muscles (c^{ii}). **c^{iii}-g**, Transverse sections show distribution of CM-DiI-positive cells between the epidermis (red dotted line) and bone (b) forming the sterlet scute (white dotted line) (c^{iii}-d, f), in epidermis (e) and in inner scute mesenchyme (f^{i}-g). **h**, Transverse section of sterlet scute show no CM-DiI signals (green) overlap with HCR expression of *col1a1* (early marker of osteoblast; blue). Every letter represents a different experimental animal. h.r., head region; not, notochord. Scale bars: 500 μm (a-b), 50 μm (b^{i}), 25 μm (c^{i}-c^{ii}), 150 μm (c^{iii}-h).

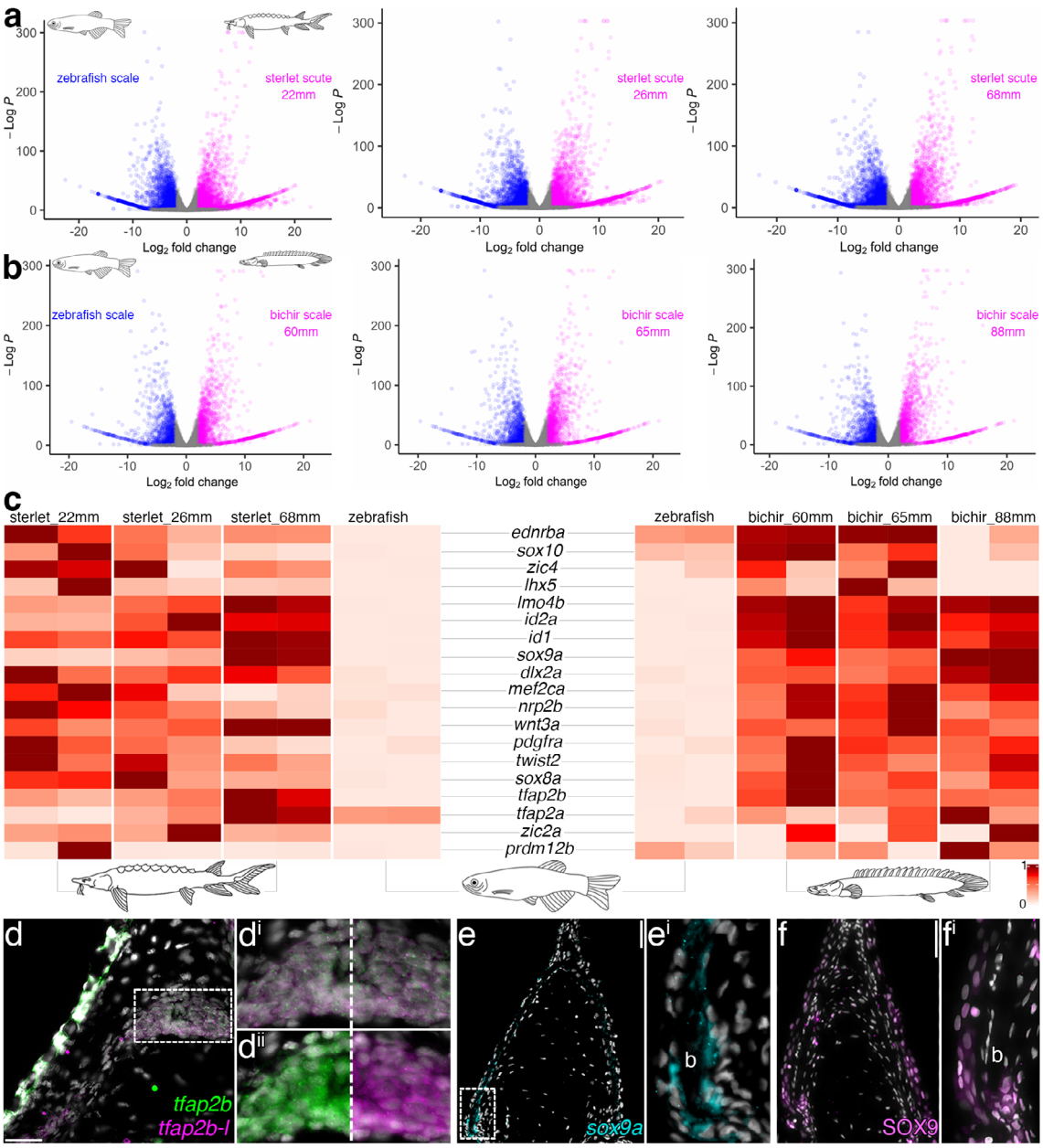

Fig. S8. RNA sequencing of dermal exoskeleton reveals enrichment of neural crest-like gene expressions in sterlet scutes and bichir ganoid scales. **a-b**, Volcano plots illustrate genes that are significantly differentially expressed (adjusted P< 0.05) between zebrafish scales (blue) and sterlet scutes (magenta) (a), and between zebrafish scales (blue) and bichir scales (magenta) (b). **c**, Hierarchical clustering analysis focused on genes identified as being part of NC GRN reveals significant enrichment of NC-like genes in sterlet scutes and bichir scales. **d-f^{i}**, Transverse sections show expression of NC-like genes in the sterlet scute. Multiplexed fluorescent mRNA *in situ* hybridizations by HCR (d-e^{i}) and antibody stainining (f-f^{i}). Scale bars: 50 μm (d-f).

Table S1. CM-DiI analyses of trunk neural crest and paraxial mesoderm contributions to sterlet scutes.

				Developmental stages (WH)						Developmental stages (sections)				
Injection target	**Total positive injections**	**Survival (%)**	**Whole-mount fluorescence (%)**	**st. 24-25**	**st. 25-27**	**st. 30**	**15 mm**	**22-23 mm**	**Total exam. in section**	**st. 24-25**	**st. 25-27**	**st. 30**	**15 mm**	**22-23 mm**
trunk NC	91	73 (80 %)	66 (90 %)	7 (st. 24)	10 (st. 25/6)	2	3	44	34	4 (st. 24)	4 (st. 25/6)	2	3	21
Paraxial mes	70	58 (82 %)	49 (84 %)	10 (st. 25)	20 (st. 26/7)	-	-	19	21	4 (st.25)	4 (st. 26/7)	-	-	13

		Distribution of CM-DiI labeled cells				
Injection target	**Total embryos sectioned at 22-23 mm**	**NT**	**Somite**	**osteoblasts**	**mesenchyme between osteoblasts and epidermis**	**internal mesenchyme**
trunk NC	21	21	0	21	0	15
Paraxial mes	13	0	13	0	5	10

Table S2. List of sterlet paralogs used in DGE analysis.

	Gene name	Gene ID	Paralog		Gene name	Gene ID	Paralog
1	**Ascl1a**	LOC117419426	Ascl1a	51	**Foxc1a-like**	LOC117394273	Foxc1a-like_1
2	**Ascl1b**	LOC117434531	Ascl1b	52	**Gata3-like**	LOC117415807	Gata3
3	**Ascl1a-like**	LOC117414484	Ascl1a-like	53	**Gata3-like**	LOC117401797	Gata2
4	**Ascl1b-like**	LOC117431927	Ascl1b-like	54	**Gata3-like**	LOC117419871	Gata3-like
14	**Col1a1-like**	LOC117973969	Col1a1-like_2	55	**Id1-like**	LOC117417627	Id1_1
15	**Col1a1-like**	LOC117434956	Col1a1-like_3	56	**Id1-like**	LOC117429566	Id1_2
16	**Col1a1-like**	LOC117396745	Col1a1-like_4	57	**Id2-like**	LOC117402271	Id2-like_1
17	**Col1a1-like**	LOC117973969	Col1a1-like_5	58	**Id2-like**	LOC117410545	Id2-like
18	**Col1a1-like**	LOC117971168	Col1a1-like_6	59	**Lmo4**	LOC117417327	Lmo4
19	**Col1a1-like**	LOC117433526	Col1a1-like_7	60	**Lmo4-a**	LOC117421866	Lmo4a
20	**Col1a1-like**	LOC117401375	Col1a1-like_8	61	**Lmo4.1-like**	LOC117396850	Lmo4.1
21	**Col9a3-like**	LOC117435728	Col9a3-like_1	62	**Lmo4-like**	LOC117402714	Lmo4-like
22	**Col9a3-like**	LOC117428480	Col9a3-like_2	63	**Msx2-like**	LOC117431417	Msx2b_1
23	**Col9a3-like**	LOC117417103	Col9a3-like_3	64	**Msx2-like**	LOC117964599	Msx2b_2
24	**Col9a3-like**	LOC117400622	Col9a3-like	65	**Msx2-like**	LOC117421465	Msx1a
26	**Destrin**	LOC117967881	Destrin	66	**Nkx1-2-like**	LOC117417878	Nkx1.2-like_1
29	**Dlx2a-like**	LOC117406003	Dlx2a_1	67	**Nkx1-2-like**	LOC117415714	Nkx1.2-like
30	**Dlx2a-like**	LOC117427121	Dlx2a_2	68	**Nkx1.2lb**	LOC117420638	Nkx1.2lb
31	**Dlx5-like**	LOC117399919	Dlx5a_1	71	**Pdgfra-like**	LOC117408343	Pdgfra_1
32	**Dlx5-like**	LOC117394322	Dlx5a_2	72	**Pdgfra-like**	LOC117420605	Pdgfra
33	**Dmbx1**	LOC117401235	Dmbx1	78	**Snai2**	LOC117394250	Snai2
34	**Dmbx1-like**	LOC117417464	Dmbx1-like	79	**Snai2-like**	LOC117425034	Snai3
35	**Dmbx1-like**	LOC117966295	Dmbx1-like_1	80	**Snai2-like**	LOC117399868	Snai2-like
36	**Dmbx1a-like**	LOC117413630	Dmbx1a-like	81	**Sox9b-like**	LOC117424573	Sox9b-like_1
37	**Ednrb**	LOC117406693	Ednrb1	82	**Sox9b-like**	LOC117423639	Sox9b-like_2
38	**Ednrb-like**	LOC117412414	Ednrb2_1	83	**Tfap2**	LOC117394948	Tfap2
39	**Ednrb-like**	LOC117405406	Ednrb1-like	84	**Tfap2-like**	LOC117399429	Tfap2-like
40	**Ednrb-like**	LOC117430294	Ednrb2_2	85	**Tfap2b**	LOC117402501	Tfap2b
41	**Ednrb-like**	LOC117421248	Ednra	86	**Tfap2b-like**	LOC117410352	Tfap2b-like
42	**Enc1**	LOC117973440	Enc1_1	91	**Twist1b**	LOC117395010	Twist1b
43	**Enc1**	LOC117403735	Enc1_2	92	**Twist2-like**	LOC117400927	Twist3a
44	**Enc1-like**	LOC117428837	Enc3	93	**Twist2-like**	LOC117427115	Twist2_1
45	**Enc1-like**	LOC117966279	Enc3	94	**Twist2-like**	LOC117967056	Twist3b
46	**FoxD1**	LOC117401948	FoxD1	95	**Twist2-like**	LOC117405956	Twist2_2
47	**FoxD1-like**	LOC117966831	FoxD1-like_1	96	**Wnt3a**	LOC117435784	Wnt3a_1
48	**FoxD1-like**	LOC117964168	FoxD1-like_1	97	**Wnt3a**	LOC117400591	Wnt3a_2
49	**FoxD1-like**	LOC117404135	FoxD1-like	98	**Zic2-like**	LOC117406673	Zic2_1
50	**Foxc1a-like**	LOC117399906	Foxc1a-like	99	**Zic2-like**	LOC117405280	Zic2_2
				100	**zic4-like**	LOC117417285	Zic4_1

101	**zic4-like**	LOC117412091	Zic6
102	**zic4-like**	LOC117430741	Zic6
103	**zic4-like**	LOC117423007	Zic4_2

Movie S1. 3D reconstruction of bichir ganoid scale.

Movie S2. 3D reconstruction of gar ganoid scale.

Movie S3. 3D reconstruction of bristlenose catfish scute.

Movie S4. 3D reconstruction of sterlet sturgeon scute.

Dataset S1. Alignment percentage scores for Sturgeon/Zebrafish alignment.

Dataset S2. Alignment percentage scores for Bichir/Zebrafish alignment.